

RESEARCH ARTICLE

10.1002/2014JA019929

This article is a companion
 to Wilson et al. [2014],
 doi:10.1002/2014JA019930.

Key Points:

- High-frequency electric fields are much larger than quasi-static fields
- They produce more energy dissipation than the quasi-static fields
- Most energy dissipation pathways end with wave-particle interactions

Correspondence to:

L. B. Wilson III,
 lynn.b.wilsoniii@gmail.com

Citation:

Wilson, L. B., III, D. G. Sibeck, A. W. Breneman, O. Le Contel, C. Cully, D. L. Turner, V. Angelopoulos, and D. M. Malaspina (2014), Quantified energy dissipation rates in the terrestrial bow shock: 1. Analysis techniques and methodology, *J. Geophys. Res. Space Physics*, 119, 6455–6474, doi:10.1002/2014JA019929.

Received 4 MAR 2014

Accepted 23 JUL 2014

Accepted article online 29 JUL 2014

Published online 25 AUG 2014

Corrected 5 JUL 2017

This article was corrected on 5 JUL 2017. See the end of the full text for details.

Different dissipation mechanisms, e.g.: wave-particle interactions and particle reflection.

Fast mode Mach number

M_f , θ_{Bn} , β

Quantified energy dissipation rates in the terrestrial bow shock: 1. Analysis techniques and methodology

L. B. Wilson III¹, D. G. Sibeck¹, A. W. Breneman², O. Le Contel³, C. Cully⁴, D. L. Turner⁵, V. Angelopoulos⁵, and D. M. Malaspina⁶

¹NASA Goddard Space Flight Center, Greenbelt, Maryland, USA, ²School of Physics and Astronomy, University of Minnesota, Minneapolis, Minnesota, USA, ³Laboratoire de Physique des Plasmas, Ecole Polytechnique, Palaiseau, France, ⁴Department of Physics and Astronomy, University of Calgary, Calgary, Alberta, Canada, ⁵Institute of Geophysics and Planetary Physics/Earth and Space Sciences, University of California, Los Angeles, California, USA, ⁶Laboratory for Atmospheric and Space Physics, University of Colorado Boulder, Boulder, Colorado, USA

Abstract We present a detailed outline and discussion of the analysis techniques used to compare the relevance of different energy dissipation mechanisms at collisionless shock waves. We show that the low-frequency, quasi-static fields contribute less to ohmic energy dissipation, $(-\mathbf{j} \cdot \mathbf{E})$, than their high-frequency counterparts. In fact, we found that high-frequency, large-amplitude (>100 mV/m and/or >1 nT) waves are ubiquitous in the transition region of collisionless shocks. We quantitatively show that their fields, through wave-particle interactions, cause enough energy dissipation to regulate the global structure of collisionless shocks. The purpose of this paper, part one of two, is to outline and describe in detail the background, analysis techniques, and theoretical motivation for our new results presented in the companion paper. The companion paper presents the results of our quantitative energy dissipation rate estimates and discusses the implications. Together, the two manuscripts present the first study quantifying the contribution that high-frequency waves provide, through wave-particle interactions, to the total energy dissipation budget of collisionless shock waves.

1. Introduction

Shock waves, in their simplest form, are discontinuities that result from the balance between nonlinear wave steepening and energy loss. The energy loss must transform the incident bulk flow kinetic energy to some other form like random kinetic energy (i.e., heat). The initiation of a shock discontinuity from a nonlinearly steepened wave requires that the energy dissipation be irreversible [Petschek, 1958; Fishman et al., 1960; Shu, 1992]. In a collision-dominated neutral media like the Earth's atmosphere, energy dissipation is accomplished through binary particle collisions. Similar processes can occur in ionized gases, but here Coulomb collisions between electrons and ions replace binary particle collisions [Spitzer and Härm, 1953]. In both neutral and ionized gases, the collisions have an effect that is analogous to an effective friction or drag force resulting in heating.

The solar wind and terrestrial bow shock are so tenuous that Coulomb collisions occur too infrequently to significantly alter the incident bulk flow kinetic energy to produce a shock discontinuity. This led to the prediction of a collisionless bow shock [Kellogg, 1962] that dissipated energy through other mechanisms. Four energy dissipation mechanisms have been proposed: dispersive radiation [e.g., Tidman and Northrop, 1968; Mellott and Greenstadt, 1984; Krasnoselskikh et al., 2002; Sundkvist et al., 2012], wave-particle interactions [e.g., Sagdeev, 1966; Gary, 1981], particle reflection [e.g., Edmiston and Kennel, 1984; Kennel et al., 1985; Kennel, 1987; Bale et al., 2005; Su et al., 2012], and macroscopic quasi-static field effects [e.g., Scudder et al., 1986a, 1986b, 1986c]. Note that the latter two mechanisms are actually thought to be the first part of a two-part process in dissipating necessary energy to maintain a stable shock ramp [e.g., Coroniti, 1970; Kennel et al., 1985; Treumann, 2009]. The relative importance of each possible energy dissipation mechanism is not well understood.

Theory [e.g., Sagdeev, 1966; Coroniti, 1970; Tidman and Krall, 1971; Wu et al., 1984; Kennel et al., 1985; Treumann, 2009] predicts that the energy dissipation occurs in a thin spatial region (shock ramp) separating upstream from the downstream and depends strongly upon fast mode Mach number, M_f , the angle, θ_{Bn} , between the average upstream magnetic field and the shock normal vector, \hat{n} , and the ratio of particle to

Low Mach number shocks: dispersive radiation and wave-particle interaction.

High Mach number: Reflection also.

Dissipation normally ends with microscopic processes involving wave-particle interactions.

Whistler precursors

Macroscopic quasi-static E and B fields are conservative, but can lead to dissipation through multistep processes.

Quasi-static E ~10 mV/m

High-frequency E ~200 mV/m

magnetic pressures called the plasma beta, β . A collisionless shock is defined as a quasi-perpendicular or quasi-parallel for $\theta_{Bn} > 45^\circ$ or $\leq 45^\circ$, respectively. At low M_r , theory suggests that the dominant mechanisms are **dispersive radiation and/or wave-particle interactions** [e.g., Kennel et al., 1985]. Theory [e.g., Edmiston and Kennel, 1984; Kennel et al., 1985] predicted that when the downstream flow speed along \hat{n} ($\langle U_{shn} \rangle_{down}$) was equal to the downstream ion-acoustic speed, known as the first critical Mach number or $M_{cr,1}$, no purely resistive shock can exist in resistive MHD. When $\langle U_{shn} \rangle_{down}$ equals or exceeds the downstream isothermal sound speed, known as the second critical Mach number or $M_{cr,2}$, particle reflection is necessary to maintain a stationary shock wave [e.g., Kennel et al., 1985; Kennel, 1987]. However, the **relative importance of each possible dissipation mechanism has not been quantified in observational studies.**

There are multiple pathways in which energy dissipation can occur in a collisionless shock, but nearly all end with microscopic processes involving wave-particle interactions. In the following, we will outline these pathways. If the shock ramp dispersively radiates a **magnetosonic whistler mode precursor** [e.g., Tidman and Northrop, 1968; Hoppe et al., 1981; Krauss-Varban and Omid, 1991], the precursor can interact with the incident upstream particles directly or indirectly, in addition to carrying (wave) energy/momentum away from the shock ramp as Poynting flux [e.g., Sundkvist et al., 2012]. The precursors can directly dissipate energy by **heating the ions perpendicular** to the quasi-static magnetic field (B_o) and/or **accelerating the electrons parallel** to B_o [e.g., Cairns and McMillan, 2005; Wilson et al., 2012]. The precursors can **indirectly dissipate energy through the generation of higher-frequency waves** by producing electron temperature anisotropy [e.g., Hull et al., 2012] or localized current-driven instabilities [e.g., Sagdeev, 1966; Gary, 1981].

Macroscopic quasi-static electric and magnetic fields are by definition conservative [e.g., Bryant, 1999]. However, they can lead to energy dissipation through multistep processes. If we view a shock ramp in a frame where the gradient in B_o is at rest over long time scales, incident electrons and ions will experience a differential acceleration due to differences in mass and sign of their electric charge. A local **charge separation** across the shock ramp arises that results in a quasi-static electric potential ($\Delta\Phi$), known as the **cross-shock potential, in order to maintain quasi-neutrality.** The electrostatic electric field associated with $\Delta\Phi$ acts to accelerate electrons into the downstream and reflects a small fraction of incident ions back into the upstream [e.g., Eastwood et al., 2007; Dimmock et al., 2012; Mitchell et al., 2012]. The combined effects of the gradient in B_o and $\Delta\Phi$ result in a competition between electron mirroring, ion reflection, and direct transmission of both species through the ramp. The shock attempts to remain stationary which requires zero current along the shock normal vector which implies that $\Delta\Phi \propto \Delta B_o$ [e.g., Hull et al., 1998, 2000, 2001]. We should note, however, that simulations suggest that this process is not necessarily stationary and that the shock can **cyclically reform** [e.g., Hellinger et al., 2007; Yang et al., 2011; Su et al., 2012]. The **reformation can occur due to an accumulation of reflected ions near the shock ramp resulting in bursts sent into the upstream.**

Note the following consequences of such a scenario: (1) the differential acceleration of incident particles will result in currents, which add to the gradient in B_o in the shock ramp; (2) Liouville mapping of electron velocity distributions predict inaccessible voids in phase space in the downstream distributions; and (3) the reflected ions have a relative drift between the incident electrons and ions, i.e., a current. Thus, the ramp currents [e.g., Sagdeev, 1966; Gary, 1981], **voids in electron velocity distributions** [e.g., Hull et al., 1998, 2000, 2001; Mitchell and Schwartz, 2014], and **reflected ion currents** [e.g., Scholer et al., 2003; Tsubouchi and Lembège, 2004; Matsukiyo and Scholer, 2006; Muschietti and Lembège, 2013] are all capable of producing **instabilities that radiate electromagnetic waves.**

Previous studies of the **quasi-static electric fields that result in $\Delta\Phi$ were often under-sampled** and had magnitudes typically only **~few tens of mV/m** [e.g., Eastwood et al., 2007; Dimmock et al., 2012]. These studies did not focus on or measure the high-frequency fields responsible for wave-particle interactions. However, they often invoke these microscopic processes as a mechanism to fill in the unobserved inaccessible voids in phase space predicted by Liouville mapping [e.g., Hull et al., 1998, 2000, 2001; Schwartz et al., 2011; Mitchell and Schwartz, 2014]. Note that the quasi-static fields studies were often able to explain the average characteristics in the downstream electron velocity distributions. However, this is not surprising if the quasi-static fields lead to the pathways we described earlier.

For comparison, **high-frequency waves** have been observed to have electric fields **$\gtrsim 200$ mV/m** [e.g., Wilson et al., 2007, 2010; Mozer and Sundkvist, 2013; Breneman et al., 2013], easily exceeding quasi-static electric field amplitudes. In addition, **no observational study has quantified the effects of wave-particle interactions**

Fluctuating electric fields cause the wave-particle interactions that act on the current.

in the global energy dissipation budget of collisionless shock waves. Therefore, we will focus on the energy dissipation produced by wave-particle interactions, through $(-\mathbf{j} \cdot \mathbf{E})$, and compare these values to macroscopic energy dissipation estimates. Note that the fluctuating electric fields that cause the wave-particle interactions act on the current. Thus, whether the fluctuating electric fields interact more efficiently with either species is not necessarily important, so long as the interaction influences their relative drift and ultimately the current. Thus, the main purpose of this study is to quantify the contribution that high-frequency waves provide, through wave-particle interactions, to the total energy dissipation budget of collisionless shock waves.

In this paper we describe the background, analysis techniques, and theoretical motivation for the results presented in the companion paper by Wilson *et al.* [2014] (from herein called Paper II). To avoid confusion, all figures and tables from this paper will be prefaced by "I:" and those from Paper II by "II:".

The paper is outlined as follows: Section 2 introduces the data sets used in this study; section 3 discusses our Rankine-Hugoniot analysis and defines the relevant coordinate bases and reference frames used in this study; section 4 discusses our comparison between quasi-static and fluctuating electric field measurements; section 5 discusses our method for estimating the current density; section 6 discusses how we quantifiably compare macroscopic with microscopic energy dissipation estimates; and section 7 summarizes the conclusions drawn from our analysis. In addition, we included appendices to provide the reader with more detailed discussions of our macroscopic (Appendix A) and microscopic (Appendix B) energy dissipation estimates and particle velocity moment (Appendix C) analysis.

2. Data Sets

In this section we introduce and describe the Time History of Events and Macroscale Interactions during Substorms (THEMIS) data sets used to examine the 11 bow shock crossings presented herein. We selected bow shock crossings where a single THEMIS spacecraft had both wave burst electromagnetic field data and particle burst velocity distributions during the shock transition. Detailed discussions of Rankine-Hugoniot analysis, critical Mach number calculations, reference frame transformations, and coordinate bases definitions are presented in section 3.

Throughout this paper we use the terms "DC-coupled" and "AC-coupled" which are determined by an instrument response. If the instrument can respond to quasi-static fields, then we refer to that as a DC-coupled quantity. If the instrument cannot respond to quasi-static fields, then we refer to that as an AC-coupled quantity. The majority of the DC-coupled electromagnetic field measurements made by THEMIS are observed at ≤ 128 samples per second (sps). However, the electric field instrument can be DC-coupled even when sampling at ~ 8192 sps. Throughout this paper the following notations are used: Q_o , δQ , and $\langle Q \rangle_{\text{region}}$, where Q_o is any DC-coupled quantity observed at ≤ 128 sps, δQ is any AC-coupled quantity observed at ~ 8192 sps, and $\langle Q \rangle_{\text{region}}$ is the average of any background parameter, Q , over the upstream or downstream regions. Note that all δQ quantities are reported at ~ 8192 sps with a single pole high-pass filter above ~ 10 Hz.

We should note that the distinction between Q_o and δQ is not the same as that typically used in theoretical studies. For instance, in quasi-linear theory, one typically assumes $Q \approx Q_o + \delta Q$ and that $\langle Q_o \rangle = Q_o$ and $\langle \delta Q \rangle = 0$, where $\langle \rangle$ represents an ensemble average. The choice of which ensemble average is chosen for physically significant reasons (e.g., choose to average over frequencies for a spectrum of waves) [e.g., Penrose, 1979]. Regardless, our use of Q_o and δQ are dependent upon the response of instruments, not the assumption that $\langle \delta Q \rangle = 0$. For instance, we will show examples herein and in Paper II where $\langle \delta Q \rangle \neq 0$.

We utilized the THEMIS fluxgate magnetometer (FGM) [Auster *et al.*, 2008] for quasi-static (DC-coupled) vector magnetic field measurements. The THEMIS FGM data returned three quasi-static magnetic field components, $B_{o,j}$, at ~ 128 sps for short durations and nearly continuous measurements at 4 sps. The FGM results were used to define the ramp (transition) region of the shocks, the Rankine-Hugoniot analysis (see section 3.1), and current density estimations (see section 5).

Waveform burst captures were obtained from the Search Coil Magnetometer (SCM) [Le Contel *et al.*, 2008; Roux *et al.*, 2008] and the Electric Field Instrument (EFI) [Bonnell *et al.*, 2008; Cully *et al.*, 2008]. The EFI(SCM) receiver returned three electric(magnetic) field components, $\delta E_j(\delta B_j)$, at a nominal sample rate of $\sim 16,384(\sim 8192)$ sps, or a Nyquist frequency of $\sim 8192(\sim 4096)$ Hz. Even when in an AC-coupled mode,

FGM used to define ramp transition

THEMIS: Also 3D E

Table 1: Shock Parameters and Rankine-Hugoniot Solutions

| Date (yyyy-mm-dd) | Probe | $ V_{shn} $ (km/s) | $ U_{shn} $ (km/s) | θ_{Bn} (deg) | M_f | $\langle N_i \rangle_{down} / \langle N_i \rangle_{up}$ |
|------------------------------|-------|-----------------------|-----------------------|------------------------|-----------------|---|
| 2009-07-13 [First crossing] | B | 53 ± 2 | 275 ± 2 | $43^\circ \pm 5^\circ$ | 3.11 ± 0.10 | 6.7 ± 0.6 |
| 2009-07-21 [First crossing] | C | 24 ± 7 | 200 ± 2 | $51^\circ \pm 6^\circ$ | 2.12 ± 0.13 | 3.6 ± 0.5 |
| 2009-07-23 [First crossing] | C | 65 ± 7 | 425 ± 2 | $83^\circ \pm 3^\circ$ | 3.05 ± 0.04 | 4.1 ± 0.3 |
| 2009-07-23 [Second crossing] | C | 13 ± 7 | 504 ± 2 | $88^\circ \pm 2^\circ$ | 3.61 ± 0.05 | 3.7 ± 0.2 |
| 2009-07-23 [Third crossing] | C | 38 ± 10 | 417 ± 1 | $54^\circ \pm 4^\circ$ | 3.12 ± 0.06 | 2.8 ± 0.4 |
| 2009-09-05 [First crossing] | C | 78 ± 5 | 270 ± 1 | $73^\circ \pm 3^\circ$ | 4.40 ± 0.06 | 6.9 ± 0.9 |
| 2009-09-05 [Second crossing] | C | 120 ± 18 | 220 ± 1 | $35^\circ \pm 2^\circ$ | 3.61 ± 0.04 | 5.4 ± 1.4 |
| 2009-09-05 [Third crossing] | C | 1 ± 16 | 357 ± 1 | $56^\circ \pm 3^\circ$ | 5.30 ± 0.06 | 6.2 ± 2.4 |
| 2009-09-26 [First crossing] | A | 29 ± 8 | 339 ± 1 | $60^\circ \pm 9^\circ$ | 4.88 ± 0.26 | 4.2 ± 0.8 |
| 2011-10-24 [First crossing] | E | 44 ± 9 | 361 ± 2 | $84^\circ \pm 5^\circ$ | 2.24 ± 0.04 | 3.0 ± 0.3 |
| 2011-10-24 [Second crossing] | E | 32 ± 5 | 365 ± 2 | $88^\circ \pm 2^\circ$ | 2.31 ± 0.01 | 4.8 ± 0.3 |

the data returned by the EFI can still be contaminated by spin-dependent photoelectron emissions and electrostatic wake effects [Bonnell et al., 2008]. Therefore, we removed any interval that showed remnant contamination prior to further analysis.

The THEMIS electrostatic analyzers (ESA) [McFadden et al., 2008a, 2008b] provide full 4π steradian particle velocity distribution functions for both electrons and ions ranging from a few eV to over 25 keV every spin period (~ 3 s) in burst mode. We refer to the electron and ion detectors as EESA and IESA, respectively. The ESA particle velocity distribution functions were used to calculate the following particle velocity moments: plasma number density, N_i ; bulk flow velocity, \mathbf{V}_{bulk} ; average ion temperature, T_i ; and average electron temperature, T_e .

3. Analysis and Methodology

In this section we describe our Rankine-Hugoniot analysis, critical Mach number estimates, reference frame transformations, and coordinate bases used.

3.1. Rankine-Hugoniot and Critical Mach Numbers

Particle velocity moments from each instrument were used to calculate shock conservation relations, reference frame transformations, and coordinate basis rotations (see section 3.2) for the 11 THEMIS bow shock crossings examined. Removal of secondary ion species (see Appendix C) reflected from the shock, e.g., gyrating and/or gyrophase bunched ion distributions [e.g., Gurgiolo et al., 1981; Meziane et al., 1997], is necessary in each event to approximate the velocity moments of the undisturbed upstream solar wind.

We numerically solved the Rankine-Hugoniot relations [e.g., Vinas and Scudder, 1986; Koval and Szabo, 2008] for each bow shock crossing in Table 1:1. These equations predict the relationship between upstream (not shocked) and downstream (shocked) bulk plasma properties. These solutions allow us to estimate the shock normal vector (\hat{n}), the upstream shock normal velocity in the spacecraft frame (V_{shn}), the upstream shock normal velocity in the shock rest frame (U_{shn}), the upstream shock normal angle (θ_{Bn}), the upstream fast mode Mach number (M_f), and the shock compression ratio ($\langle N_i \rangle_{down} / \langle N_i \rangle_{up}$). We use these parameters to characterize the macroscopic properties of the shock (see Appendix A).

The results of the Rankine-Hugoniot analysis can be seen in Table 1:1. As one can see, two of the crossings were classified as quasi-parallel while the rest were quasi-perpendicular and all the shocks were low-to-mid Mach number with $M_f \sim 2$ –6.

For each crossing, we estimated four so-called critical Mach numbers, where the ratios can be seen in Table 1:2. We estimated two critical Mach numbers, $M_{cr,1}$ and $M_{cr,2}$, which are important for determining the transition from a shock dependent upon purely resistive (i.e., wave-particle interactions) effects to one that relies upon other mechanisms [Edmiston and Kennel, 1984; Kennel et al., 1985; Kennel, 1987]. There are three whistler critical Mach numbers [Krasnoselskikh et al., 2002] and are defined as follows: M_w corresponds to the maximum Mach number at which a linear whistler can phase stand with respect to the shock front; M_{gr} is the maximum Mach number which would allow a whistler wave to carry energy into the upstream; and M_{nw} is the maximum Mach number for which a stationary shock front solution can be found, above

V_{shn}

Various critical Mach numbers

Table 1: Critical Mach Number Ratios

| Date (yyyy-mm-dd) | $M_f/M_{cr,1}$ | $M_f/M_{cr,2}$ | M_f/M_w | M_f/M_{gr} | M_f/M_{nw} |
|------------------------------|-----------------|-----------------|-----------------|-----------------|-----------------|
| 2009-07-13 [First crossing] | 3.00 ± 0.11 | 2.72 ± 0.13 | 0.20 ± 0.02 | 0.15 ± 0.01 | 0.14 ± 0.01 |
| 2009-07-21 [First crossing] | 1.50 ± 0.13 | 1.18 ± 0.10 | 0.15 ± 0.02 | 0.12 ± 0.01 | 0.11 ± 0.01 |
| 2009-07-23 [First crossing] | 2.52 ± 0.08 | 2.25 ± 0.08 | 1.24 ± 0.48 | 0.95 ± 0.37 | 0.88 ± 0.34 |
| 2009-07-23 [Second crossing] | 2.97 ± 0.10 | 2.57 ± 0.10 | 5.24 ± 5.19 | 4.04 ± 4.00 | 3.71 ± 3.67 |
| 2009-07-23 [Third crossing] | 2.62 ± 0.09 | 2.35 ± 0.09 | 0.25 ± 0.02 | 0.19 ± 0.02 | 0.18 ± 0.02 |
| 2009-09-05 [First crossing] | 4.31 ± 0.05 | 3.22 ± 0.06 | 0.71 ± 0.09 | 0.55 ± 0.07 | 0.50 ± 0.06 |
| 2009-09-05 [Second crossing] | 3.51 ± 0.05 | 3.13 ± 0.15 | 0.20 ± 0.00 | 0.16 ± 0.00 | 0.14 ± 0.00 |
| 2009-09-05 [Third crossing] | 5.13 ± 0.06 | 4.67 ± 0.14 | 0.44 ± 0.03 | 0.34 ± 0.02 | 0.31 ± 0.02 |
| 2009-09-26 [First crossing] | 4.66 ± 0.33 | 4.16 ± 0.30 | 0.45 ± 0.13 | 0.35 ± 0.10 | 0.32 ± 0.09 |
| 2011-10-24 [First crossing] | 2.04 ± 0.05 | 1.67 ± 0.08 | 1.00 ± 0.75 | 0.77 ± 0.58 | 0.71 ± 0.53 |
| 2011-10-24 [Second crossing] | 1.74 ± 0.01 | 1.31 ± 0.03 | 2.58 ± 1.48 | 1.99 ± 1.14 | 1.83 ± 1.05 |

How did he compute the critical numbers?

http://www.sp.ph.ic.ac.uk/~sjs/shock_methods.pdf

which, the wave breaks. We have examined 11 THEMIS bow shock crossings, all of which satisfy $M_f/M_{cr,1}$, and $M_f/M_{cr,2} > 1$, thus, all are supercritical.

Any collisionless shock satisfying $M_f/M_{cr,2} > 1$ should, by definition, require particle reflection to dissipate sufficient energy to maintain a stationary state. In all crossings examined, we observed evidence of reflected particles (discussed in more detail in Appendix C), as predicted for $M_f/M_{cr,2} > 1$. However, evidence of reflected ions has been observed at subcritical shocks as well [e.g., Greenstadt and Mellott, 1987]. Given that previous studies [e.g., Wilson et al., 2007] found increasing high-frequency electrostatic wave amplitudes with increasing M_f , for a similar range of Mach numbers, shows that such waves persist even for $M_f/M_{cr,2} > 1$. As we discussed in section 1, reflected ions can result in unstable particle velocity distributions that drive instabilities, which can directly or indirectly excite low- and high-frequency waves. Since reflected particles ultimately result in microphysical wave-particle interactions, we did not focus on the energy loss specifically due to reflected particles.

http://www.issibern.ch/PDF-Files/analysis_methods_1_1a.pdf

3.2. Reference Frames and Coordinate Bases

In this section, we define the reference frames and coordinate bases used throughout this paper.

The first coordinate basis is a magnetic field-aligned coordinate (FAC) system where $\hat{\mathbf{z}} = \mathbf{B}_o$; $\hat{\mathbf{y}} = \mathbf{B}_o \times \hat{\mathbf{x}}_{gse}$, where $\hat{\mathbf{x}}_{gse}$ is the x axis of the geocentric solar ecliptic (GSE) coordinate basis; and $\hat{\mathbf{x}} = (\mathbf{B}_o \times \hat{\mathbf{x}}_{gse}) \times \mathbf{B}_o$.

Next, we define the transformation into the Normal Incidence Frame (NIF) and coordinate basis rotations into the Normal incidence frame Coordinate Basis (NCB) [e.g., Scudder et al., 1986a]. The NCB is defined as $\hat{\mathbf{x}} = \hat{\mathbf{n}}$; $\hat{\mathbf{y}} = \beta$; and $\hat{\mathbf{z}} = \hat{\mathbf{n}} \times \beta$, where $\beta = (\mathbf{B}_o)_{\text{down}} \times (\mathbf{B}_o)_{\text{up}}$. Note that $\hat{\mathbf{y}}$ and $\hat{\mathbf{z}}$ need to be normalized.

To transform from the spacecraft frame of reference (SCF) to the NIF, we define a transformation velocity given by $\mathbf{V}^{\text{NIF}} = \hat{\mathbf{n}} \times (\mathbf{V}_u \times \hat{\mathbf{n}})$, where $\mathbf{V}_u = \mathbf{V}_{\text{bulk}} - (V_{\text{shn}} \hat{\mathbf{n}})$. Therefore, the upstream flow velocity in the NIF and the GSE basis is given by $\mathbf{V}_u^{\text{NIF}} = \mathbf{V}_u - \mathbf{V}^{\text{NIF}}$. Thus, the frame transformation velocity, $\Delta \mathbf{V}$, between SCF and NIF is given by $\Delta \mathbf{V} = \mathbf{V}_{\text{bulk}} - \mathbf{V}_u^{\text{NIF}} = \mathbf{V}_{\text{bulk}} - [\mathbf{V}_{\text{bulk}} - (V_{\text{shn}} \hat{\mathbf{n}})] + \mathbf{V}^{\text{NIF}} = (V_{\text{shn}} \hat{\mathbf{n}}) + \mathbf{V}^{\text{NIF}}$.

Since the change in velocity between any shock rest frame to the SCF satisfies $|\beta| \equiv |\Delta \mathbf{V}|/c \ll 1$ for any shock within the heliosphere, the Lorentz transformations of the electric and magnetic fields [Jackson, 1998, p. 558] can be given by $\mathbf{E}' \approx (\mathbf{E} + \beta \times \mathbf{B})$ and $\mathbf{B}' \approx \mathbf{B}$. Therefore, we can show that the electric field in the NIF, \mathbf{E}^{NIF} , can be determined from the electric field observed in the SCF, \mathbf{E}^{SCF} , and is given by $\mathbf{E}^{\text{NIF}} = \mathbf{E}^{\text{SCF}} + (\Delta \mathbf{V} \times \mathbf{B}) = \mathbf{E}^{\text{SCF}} + [(V_{\text{shn}} \hat{\mathbf{n}} + \mathbf{V}^{\text{NIF}}) \times \mathbf{B}]$. It should be noted that this reference frame transformation, $(\Delta \mathbf{V} \times \mathbf{B})$, is rarely more than a few mV/m in magnitude. For instance, for the 26 September 2009 event, $|(\Delta \mathbf{V} \times \mathbf{B})| \lesssim 2.5$ mV/m. Comparison with low- and high-frequency electric fields (e.g., see section 4) showed that these convective frame-dependent electric fields were relatively insignificant.

4. Comparison Between \mathbf{E}_o and $\delta \mathbf{E}$

In this section we present an example bow shock crossing showing the steps necessary to clean the DC-coupled electric field data, \mathbf{E}_o . We then compare observations of \mathbf{E}_o with $\delta \mathbf{E}$ and show that $\delta \mathbf{E} \gg \mathbf{E}_o$. In section 6 we discuss the impacts of these results in our microscopic energy dissipation rate estimates.

C.f. the 1st ISSI multi-SC book, chapter 10.

\mathbf{V}_{bulk} is in arbitrary ref. system

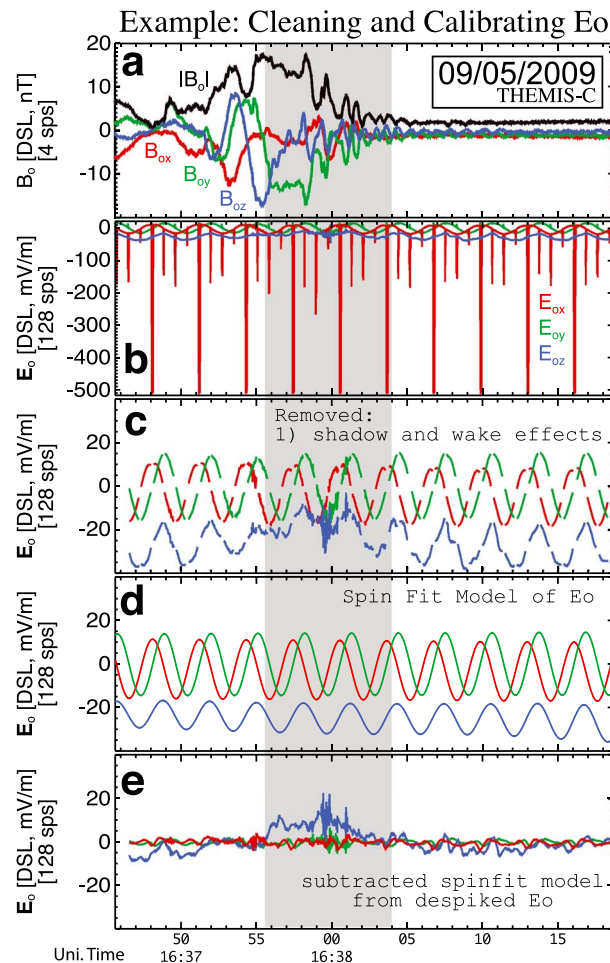


Figure I:1. This figure shows an example of the steps necessary to remove artificial signals from E_o for a bow shock crossing observed by THEMIS-C on 5 September 2009 (second crossing). The data are shown in Despun Sun-L-vectorZ or DSL coordinates, where the Z axis is along the spin axis, Y axis is orthogonal to the spin axis and the spacecraft-to-sun direction, and the X axis completes the right-hand set. The panels are as follows: (a) $|B_o|$ (nT, 4 sps, FGM) and its DSL components; (b) original level-1 E_o (mV/m, 128 sps, EFI); (c) E_o after removing shadow and wake effects; (d) model spinfit to the data in Figure I:1c; and (e) final E_o after subtracting the model in Figure I:1d. As shown in Table I:1, this shock had $M_f \sim 3.6$ and $\theta_{Bn} \sim 35^\circ$.

Figure I:1 shows the steps necessary to remove artificial signals from E_o . The large spikes in E_{ox} (red line) in Figure I:1b were due to shadow and wake effects [e.g., Bonnell *et al.*, 2008]. After these spikes were removed, it was necessary to remove remnant spin tones. The spin tones remain because the data were intentionally not despun. The large spikes shown in Figure I:1b significantly reduce the quality of the model spin fit results, which are shown in Figure I:1d. After we subtracted the model (Figure I:1d) from the “de-spiked” data (Figure I:1c), the data shown in Figure I:1e were the result.

After removing the artificial signals from E_o we compared the results with the calibrated δE data. Figure I:2 shows the comparison in the NIF and NCB. Note that $\delta E \gg E_o$, which we consistently observed in every bow shock crossing examined. It is important to note that the spiky fluctuations seen in E_o (Figure I:2b) were found to be the under-sampled fluctuations seen in δE (Figure I:2c). The majority of the quasi-static field amplitudes were attributed to magnetosonic whistler waves or the quasi-static fields in the shock ramps.

5. Current Density

In this section, we present how spatial scales and current densities are estimated. We needed the current density to estimate the microscopic energy dissipation due to the work done by the wave electric fields on the plasma per unit volume, or wave-particle interactions (discussed in

Appendix B). The microscopic energy dissipation rate, due to wave-particle interactions (see Appendix B), was compared to the macroscopic dissipation rate (defined in Appendix A) to determine if the waves can regulate the shock transition alone. The quantitative results are presented in Paper II.

5.1. Implementation

We wish to estimate the current density, $\mathbf{j}_o (= \nabla \times \mathbf{B}_o / \mu_o)$, which requires a spatial scale to substitute for ∇ . We have already determined V_{shn} (see section 3.2) from our Rankine-Hugoniot analysis. Therefore, we can use the sample period from the FGM instrument, Δt , and V_{shn} , using the “Taylor hypothesis,” to calculate an associated spatial scale $\Delta X_n \equiv V_{shn} \Delta t$. It is important to note that this assumption only works for relatively large spatial scales, and it assumes that all fluctuations are being convected at the same speed. The high-frequency waves we are interested in have spatial scales much too small to utilize multispacecraft observations. Therefore, we are limited to single-spacecraft observations and our assumption of the connection between temporal and spatial scales at low frequencies near the shock ramp.

High-frequency waves have spatial scales that are small - smaller than the MMS scale size?

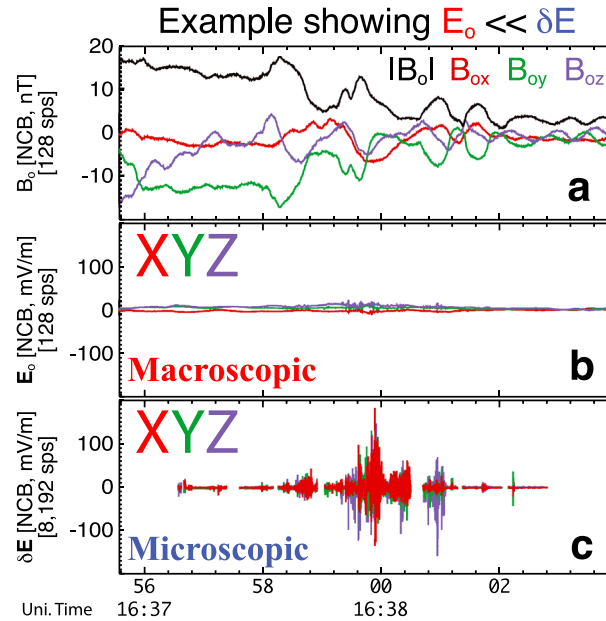


Figure I:2. This figure shows a comparison between \mathbf{E}_o and $\delta\mathbf{E}$ for the interval defined by the gray-shaded region in Figure I:1. The panels are as follows: (a) $|\mathbf{B}_o|$ (nT, 128 sps, FGM) and its NCB components; (b) \mathbf{E}_o (mV/m, 128 sps, EFI) in the NIF and NCB; and (c) $\delta\mathbf{E}$ (mV/m, 8192 sps, EFI) in the NIF and NCB. Notice that Figures I:2b and I:2c have the same vertical axis scale.

We want to calculate \mathbf{j}_o in the NIF and NCB. On this basis, V_{shn} , and thus ΔX_n , is along the $\hat{\mathbf{x}}$ component. We also know that $\nabla \cdot \mathbf{B}_o \approx \hat{\mathbf{n}} \cdot \mathbf{B}_o \approx 0$, where $\hat{\mathbf{n}}$ is the shock normal vector. If we also assume $\nabla \cdot \mathbf{j}_o \approx \hat{\mathbf{n}} \cdot \mathbf{j}_o \approx 0$, then we have $\mu_o \mathbf{j}_o = \nabla \times \mathbf{B}_o \approx -\hat{\mathbf{y}} \partial_x B_{oz} + \hat{\mathbf{z}} \partial_x B_{oy}$, which we can rewrite as follows:

$$\mathbf{j}_o \approx \frac{1}{\mu_o} \left[-\hat{\mathbf{y}} \frac{\Delta B_{oz}}{\Delta X_n} + \hat{\mathbf{z}} \frac{\Delta B_{oy}}{\Delta X_n} \right]. \quad (1)$$

We wish to compare the possible dissipation rates due to electromagnetic waves, $|\mathbf{j} \cdot \mathbf{E}|$ to our macroscopic estimate from entropy production, $\dot{\Psi} = (\langle \rho \rangle_{up} \langle T \rangle_{up}) \Delta \dot{s} / \Delta \tau$. Given that we rarely observe coherent fluctuations in \mathbf{B}_o above ~ 10 Hz (see discussion of whistler mode waves in Paper II) and that the Taylor hypothesis increases in uncertainty with increasing frequency, we smoothed our estimates of \mathbf{j}_o down to ~ 10 Hz prior to using \mathbf{j}_o to estimate $(-\mathbf{j}_o \cdot \delta\mathbf{E})$. Then we transform $\delta\mathbf{E}$ into the NIF and then rotate into the NCB. Since we

assume $\mathbf{j}_o \sim \text{constant}$ over the sample period of $\delta\mathbf{E}$ and we want to estimate the energy dissipated by high-frequency ($\gtrsim 10$ Hz) waves affecting \mathbf{j}_o , we up-sampled \mathbf{j}_o to match the time steps for $\delta\mathbf{E}$ prior to calculating $(-\mathbf{j} \cdot \mathbf{E})$. The details of these dissipation rates are discussed in the Appendix B and the details of our assumptions for calculating $(-\mathbf{j} \cdot \mathbf{E})$ are in section 5.2.

We observed that the uncertainty in $\delta\mathbf{E}$ and \mathbf{B}_o were relatively small by comparison to the parameters from our Rankine-Hugoniot results. Therefore, we believed that the uncertainties in \mathbf{j}_o would be dominated by uncertainties in V_{shn} .

To determine the relative impact of these uncertainties, we calculated ΔX_n using three variances of V_{shn} , shown in the bottom two panels in Figure I:3. Two of the three versions of ΔX_n were calculated by first subtracting (red lines) or adding (blue lines) the uncertainties in V_{shn} to V_{shn} . The third version (green lines) resulted from using V_{shn} . One can see, by examining the bottom two panels in Figure I:3, that $j_{y(z)}$ had relatively small deviations (red or blue lines) from the third version (green lines). Therefore, we argue that our estimates of \mathbf{j}_o will not introduce uncertainties significant enough to impede its use in estimating $(-\mathbf{j} \cdot \mathbf{E})$.

5.2. Approximations

In this section, we present our approximations used to calculate the current density, \mathbf{j} . Then we justify the comparison between high-frequency electric fields and low-frequency magnetic fields.

First, we assume that $\mathbf{j} \approx \mathbf{j}_o + \delta\mathbf{j}$ and $\mathbf{E} \approx \mathbf{E}_o + \delta\mathbf{E}$ so that $\mathbf{j} \cdot \mathbf{E}$ can be written as

$$\mathbf{j} \cdot \mathbf{E} \approx (\mathbf{j}_o + \delta\mathbf{j}) \cdot (\mathbf{E}_o + \delta\mathbf{E}) \quad (2a)$$

$$= (\mathbf{j}_o \cdot \mathbf{E}_o) + (\mathbf{j}_o \cdot \delta\mathbf{E}) + (\delta\mathbf{j} \cdot \mathbf{E}_o) + (\delta\mathbf{j} \cdot \delta\mathbf{E}) \quad (2b)$$

where \mathbf{E} is the measured electric field. Note that we measured and analyzed both \mathbf{E}_o and $\delta\mathbf{E}$.

The approximation $|\mathbf{j} \cdot \mathbf{E}| \sim |\mathbf{j}_o \cdot \delta\mathbf{E}|$ used in our study, which requires neglecting everything on the right-hand side of equation (2b) except the second term, was justified by our observations. The details of these arguments are as follows:

They up-sample \mathbf{j} to $\delta\mathbf{E}$!

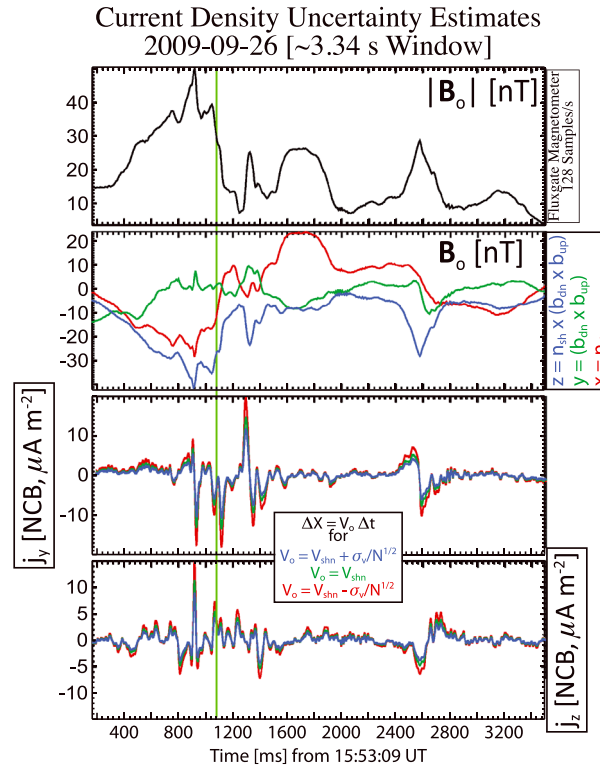


Figure I:3. This figure shows an example uncertainty calculation for j_o for the same event observed by THEMIS-A on 26 September 2009 as shown in Figure II:1 in Paper II. The top two panels show the magnitude of B_o and its NCB components. The third (fourth) panel shows three values of $j_{y(z)}$. The color-coded lines show the value of V_{shn} (see inset box) used to estimate ΔX_n for equation (1). The green vertical line indicates the center of the shock ramp at $\sim 15:53:10.080$ UT. As shown in Table I:1, this shock had $M_f \sim 4.9$ and $\theta_{Bn} \sim 60^\circ$.

1. We argue that the largest component of j should be well resolved as gradients in B_o (i.e., FGM data at ≤ 128 sps) because
 - a. we assume that the largest component of j arises from the bulk flow relative drifts between oppositely charged particle species;
 - b. these bulk drifts are responsible for the large scale changes in B_o in the shock ramp and in magnetosonic whistler waves (e.g., see Figure I:3 and Paper II);
 - c. our observations show that the majority of the largest changes in B_o occur at frequencies < 10 Hz because we do not see the corresponding δB in the SCM data filtered above 10 Hz (e.g., see Paper II);
 - d. therefore, the associated current densities should have a quasi-static response because we can clearly resolve the main shock structure with ≤ 128 sps FGM data; and
 - e. thus, we conclude that the largest contribution to j should be well resolved in B_o , which we define as j_o .
2. We argue that we can neglect the $(j_o \cdot E_o)$ term on the right-hand side of equation (2b) because we consistently observe $E_o \ll \delta E$ and $|j_o \cdot E_o| \ll |j_o \cdot \delta E|$ (see section 4).

3. We argue that we can neglect the $(\delta j \cdot E_o)$ and $(\delta j \cdot \delta E)$ terms on the right-hand side of equation (2b) because
 - a. we observed that the largest components of δE are primarily composed of electrostatic waves (see Paper II); therefore, δE should not contribute to δj . Here we assume $\mu_o \delta j = \nabla \times \delta B - c^{-2} \partial_t \delta E \sim \nabla \times \delta B$. As a figurative example, let us consider the ion-acoustic wave in Figure II:5 in Paper II. For the interval of the waveform shown, we estimate $f_{pi} \sim 590$ – 660 Hz, we know $f < f_{pi}$ from the dispersion relation for these modes, and we observe a wave amplitude ~ 40 mV/m (this is a peak-to-peak value, but we will use it anyways to estimate an upper bound). To simplify the calculations, let us assume $f \sim 500$ Hz and $c^{-2} \partial_t \delta E \sim c^{-2} \omega \delta E$. Then the contribution to δj from this ion-acoustic wave is given by $\sim (c^{-2} \mu_o^{-1} \omega \delta E) < 0.001 \mu A m^{-2}$. Below we will show that this value is much smaller than those contributed by the electromagnetic modes;
 - b. therefore (and from our first argument regarding j_o), we conclude that δj must arise from the high-frequency electromagnetic whistler mode waves (e.g., see Figure II:4 in Paper II);
 - c. typical amplitudes for whistler mode waves observed by THEMIS are $\delta B \lesssim 1.0$ nT and previous studies found wave numbers $k\rho_{ce} \sim 0.2$ – 0.8 [e.g., Wilson et al., 2013a];
 - d. thus, from these wave parameters and assuming $\rho_{ce} \sim 1$ km we can estimate a range of values for $\delta j \sim k\delta B/\mu_o \lesssim 0.2$ – $0.6 \mu A m^{-2}$;
 - e. in addition, one can estimate j_o across a shock ramp from observations showing that shock ramps have $\Delta B_o \sim 10$ – 30 nT and gradient scale lengths, $L_{sh} \sim 2 c/\omega_{pe} - 1 c/\omega_{pi}$ [e.g., Mazelle et al., 2010], which corresponds to $j_o \sim \Delta B_o/(\mu_o L_{sh}) \sim 0.2$ – $12 \mu A m^{-2}$ (assuming $c/\omega_{pe} \sim 1$ km);
 - f. these estimates combined with observations (e.g., see Figure I:3) consistently showed $j_o \gg \delta j$;

Can I test this? Does the curlometer method work on SCM data?

- g. therefore, because $j_o \gg \delta j$ and $E_o \ll \delta E$, we argue that $|\delta \mathbf{j} \cdot \mathbf{E}_o| \ll |\mathbf{j}_o \cdot \delta \mathbf{E}|$;
- h. we consistently observed that δE from the whistlers was much smaller than from the electrostatic waves and $j_o \gg \delta j$; therefore
- i. we argue that $|\delta \mathbf{j} \cdot \delta \mathbf{E}| \ll |\mathbf{j}_o \cdot \delta \mathbf{E}|$.

These approximations allow to reduce equation (2b) to $(-\mathbf{j} \cdot \mathbf{E}) \sim (-\mathbf{j}_o \cdot \delta \mathbf{E})$, which supports the arguments presented in section 5.1. Therefore, the contribution to the rate of energy dissipation per unit volume from the electric fields is dominated by the high-frequency electrostatic waves focused on in Paper II.

Ideas behind up-sampling J.

Since \mathbf{j}_o varies much more slowly than $\delta \mathbf{E}$, we can assume $\mathbf{j}_o \sim \text{constant}$ over the typical wave periods observed in $\delta \mathbf{E}$. Therefore, we can up-sample \mathbf{j}_o to the $\delta \mathbf{E}$ time steps without significantly compromising our results.

6. Macroscopic Versus Microscopic Dissipation

Cumulative sum? Not integral?

In this section we compare the microscopic energy dissipation rates, due to wave-particle interactions, $(-\mathbf{j}_o \cdot \mathbf{E}_o)$ with $(-\mathbf{j}_o \cdot \delta \mathbf{E})$ and cumulative sum of the microscopic energy dissipation rates. To quantify the relative impact of the wave energy dissipation rate, we compare the microscopic (e.g., wave-particle interactions) to the macroscopic (e.g., increase in entropy) dissipation rates.

Before discussing our estimates of energy dissipation, we should point out that the electric and magnetic field data examined in our manuscript represent a signal that has had multiple low-pass filters applied with the intent of removing wave power above the Nyquist frequency (1/2 the sample rate). These anti-aliasing filters ensure that the measured field value is stable during a single sample digitization interval. Therefore, the field measurements are only instantaneous in the sense that they represent fluctuations in the true field below the Nyquist frequency at a given time. Any wave power contained in frequencies above the Nyquist frequency is not measured. Taking a time average of a time series is similar to performing a low-pass filter in that it removes higher frequencies from the signal (though often not as uniformly as other low-pass filters). If there is substantial wave power at high frequencies, an average will remove it. Thus, even though the EFI can sample up to $\sim 16,384$ sps, this is not “instantaneous.” Though we used this term in section 5, it is used with instrumental constraints kept in mind.

Cumulative sum? Not integral?
Note that the cumulative sum will be proportional to the number of samples!

Figure I:4 shows a comparison between the energy dissipation rates due to \mathbf{E}_o and those due to $\delta \mathbf{E}$. The direct estimate of the dissipation rates are shown in panel Figure I:4c, while the respective cumulative sums are shown in Figure I:4d. Note that these are plotted on the same scale. We found that not only was $|\mathbf{j}_o \cdot \delta \mathbf{E}| \gg |\mathbf{j}_o \cdot \mathbf{E}_o|$ satisfied, the cumulative sums corroborated. The first relationship was expected, since we consistently observed $\delta E \gg E_o$. The much larger cumulative sum for δE supports our argument that $(-\mathbf{j} \cdot \mathbf{E}) \sim (-\mathbf{j}_o \cdot \delta \mathbf{E})$ in section 5.

Cumulative sum: net amount of work

The purpose of using the cumulative sum for the $(-\mathbf{j} \cdot \mathbf{E})$ terms was to test whether the electric fields could contribute a net amount of work to the plasma. We do this rather than imposing an arbitrary time scale when estimating a time average. However, in Figure I:4e we show multiple time averages using a box-car average. The number of points for each time average is shown in the box in the left-hand portion of Figure I:4e, where the label colors correspond with the line colors. As one can see, as we increase the number of points over which we average our signal, the amplitude decreases. The decrease in amplitude is expected because any time average of a signal acts similarly to a low-pass frequency filter, thus removing amplitude from the signal. Therefore, the smaller amplitudes shown in Figure I:4e compared to Figure I:4c result from the removal of power at higher frequencies, which negates the purpose of using high time resolution measurements.

Of course, signal decreases when averaging

There are multiple issues with performing a time average on a time series of data. In quasi-linear theory, when assuming a system is ergodic, the use of a time average works because the system is not expected to deviate significantly from its expectation value, which roughly corresponds to a time average. However, as explained by Penrose [1979], using a time average instead of an ensemble average poses serious issues such as the following: (1) it precludes the possibility for nonequilibrium phenomena; (2) all measurements are discrete while time averages assume infinite times; and (3) it “gives no rationale for excluding ‘exceptional’ motions.” For example, suppose a constant current existed spatially and temporally collocated with a fluctuating sinusoidal electric field. Then one might expect that the time average of $(-\mathbf{j} \cdot \mathbf{E}) \sim 0$. In other words, the oscillating electric fields would only cause a periodic variation in the particle distributions, but

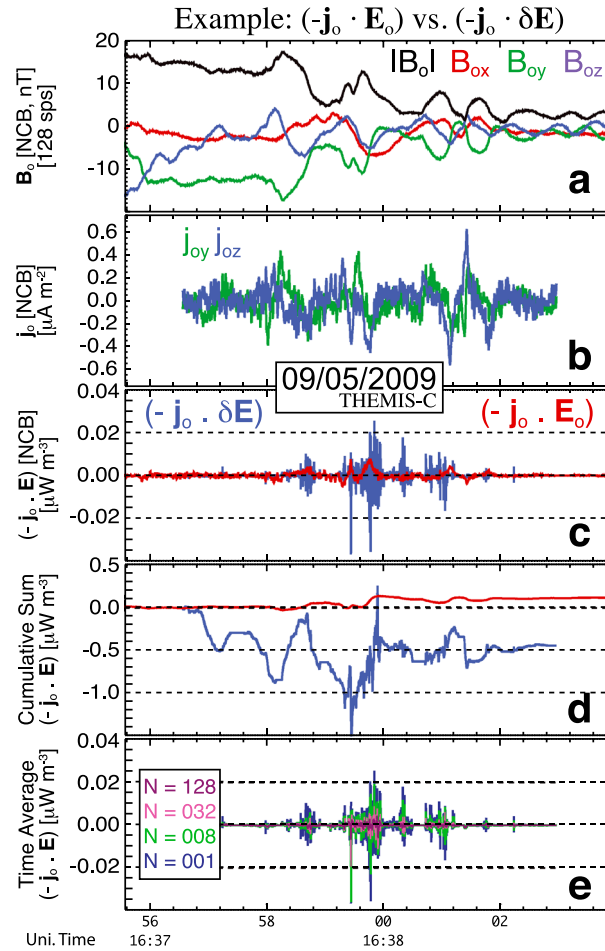


Figure I:4. This is the same as Figure I:2, but compares the energy dissipation rates due to $(-\mathbf{j}_o \cdot \mathbf{E}_o)$ versus $(-\mathbf{j}_o \cdot \delta \mathbf{E})$. The panels are as follows: (a) $|\mathbf{B}_o|$ (nT, 128 sps, FGM) and its NCB components; (b) two NCB components of the current density, \mathbf{j}_o ($\mu A m^{-2}$); (c) $(-\mathbf{j} \cdot \mathbf{E})$ for quasi-static macroscopic fields (red line) and fluctuating microscopic fields (blue line) ($\mu W m^{-3}$); (d) the cumulative sum of the data in Figure I:4c; and (e) multiple time-averages of the data in Figure I:4c. For reference, the dark blue ($N = 001$) line corresponds to the original signal (blue line) in Figure I:4c. The new effective sample rates associated with each N are: ($N = 001$) $\equiv 8192$ sps; ($N = 008$) $\equiv 1024$ sps; ($N = 032$) $\equiv 256$ sps; and ($N = 128$) $\equiv 64$ sps.

by $(-\eta_{wave} |\mathbf{j}_o|^2)$. Therefore, to quantify the relative importance of wave-particle interactions to the total shock energy dissipation budget, we define the following unitless ratios:

$$\mathcal{R}_\Psi \equiv \frac{|\mathbf{j}_o \cdot \delta \mathbf{E}|}{\dot{\Psi}} \quad (3a)$$

$$\mathcal{T}_\Psi \equiv \frac{|\mathbf{j}_o \cdot \delta \mathbf{E}|}{\dot{\kappa}} \quad (3b)$$

$$\mathcal{Y}_\Psi \equiv \frac{\eta_{iaw} |\mathbf{j}_o|^2}{\dot{\Psi}} \quad (3c)$$

$$\mathcal{Z}_\Psi \equiv \frac{\eta_{iaw} |\mathbf{j}_o|^2}{\dot{\kappa}} \quad (3d)$$

where we have used equation (A2) for $\dot{\Psi}$ and equation (A3) for $\dot{\kappa}$.

Note, that when \mathcal{R}_Ψ or $\mathcal{Y}_\Psi > 1$, then the microscopic electromagnetic energy dissipation exceeds the amount of macroscopic fluid energy dissipation necessary to explain the changes in entropy across the

could not transfer a net amount of energy/momentum, through work, to the particles. Figure I:4d shows that both \mathbf{E}_o and $\delta \mathbf{E}$ produced a net change in $(-\mathbf{j} \cdot \mathbf{E})$ across the shock ramp. In addition, Lapenta et al. [2014] recently provided a useful comment on the subject of time averages: "Average is a dangerous concept as a hungry person would readily testify watching someone eating two servings. The fact that on average as many particles gain energy as others lose energy does not mean that no energy is being exchanged..."

The positive sign associated with $(-\mathbf{j}_o \cdot \mathbf{E}_o)$, the red line, in Figure I:4d implies that the particles are losing energy/momentum at the expense of an increasing electromagnetic energy density or flux. As we discussed earlier and will discuss in Paper II, we believe that the quasi-static fields act to differentially decelerate the incident bulk flow, while the high-frequency fluctuations increase the average kinetic energy in the bulk flow rest frame of the particles, i.e., heat.

In summary, we consistently observe the following in every bow shock crossing examined: $\delta E \gg E_o$; $|\mathbf{j}_o \cdot \delta \mathbf{E}| \gg |\mathbf{j}_o \cdot \mathbf{E}_o|$; and their respective cumulative sums. We argue in Paper II that wave-particle interactions, due to high-frequency waves in low-to-mid Mach number collisionless shocks, are the dominant form of energy dissipation.

In section 5 and Appendix B we showed that the energy dissipation rate due to wave-particle interactions was given by $(-\mathbf{j}_o \cdot \delta \mathbf{E})$. In Appendix B we provided a supplemental approximation to this, given

Panel d: It looks like red and blue step up and down coincide at medium scale, but over the entire interval they differ.

Right column:
Quasi-static field decelerate.
High-frequency fields heat.

shock ramp. Therefore, we focused on these ratios and show that high-frequency electromagnetic waves play a significant role in the global energy budget of low Mach number collisionless shocks (see Paper II for quantitative results).

7. Discussion and Conclusions

The work presented herein can be summarized by the following points:

1. We consistently observe the following in every THEMIS bow shock crossing examined:
 - a. $\delta E \gg E_o$;
 - b. $|\mathbf{j}_o \cdot \delta \mathbf{E}| \gg |\mathbf{j}_o \cdot \mathbf{E}_o|$; and
 - c. the magnitude of the cumulative sum of $(-\mathbf{j}_o \cdot \delta \mathbf{E})$ was much larger than for $(-\mathbf{j}_o \cdot \mathbf{E}_o)$.
2. We observe evidence for particle reflection in every THEMIS bow shock crossing examined (e.g., see Appendix C for details). The reflected particles are consistent with gyrating, field-aligned beam, and intermediate/diffuse ions [e.g., Paschmann et al., 1981]. The total relative density of the reflected particles ranged from ~ 20 to 40% , while the beam-like ions only composed ~ 1 – 5% . While these relative densities are high, there are a few important things to take note of:
 - a. intermediate/diffuse ions are thought to be the free energy source for shocklets and short large-amplitude magnetic structures [e.g., Scholer et al., 2003; Tsubouchi and Lembège, 2004], which can locally produce \mathbf{j}_o due to the associated gradients in \mathbf{B}_o ;
 - b. the relative drift between reflected ions and incident electrons (e.g., a current) can provide the free energy for an instability responsible for one of the high-frequency waves of interest (discussed in Paper II) [e.g., Matsukiyo and Scholer, 2006; Muschietti and Lembège, 2013];
 - c. reflected ions, if transmitted into the downstream as a gyrating ring, could excite Alfvén ion cyclotron waves [e.g., Davidson and Ogden, 1975] and other electromagnetic waves [e.g., Lu and Wang, 2006; Hao et al., 2014];
 - d. if the reflected ions generate low-frequency waves, then they contribute to our dissipation estimates through \mathbf{j}_o ;
 - e. if the reflected ions generate high-frequency waves, then they contribute to our dissipation estimates through both \mathbf{j}_o and $\delta \mathbf{E}$.
3. Thus, our estimates of $(-\mathbf{j}_o \cdot \delta \mathbf{E})$ are still relevant because they can include effects from particle reflection directly or indirectly.

In summary, we have shown that the high-frequency waves consistently satisfy $\delta E \gg E_o$ and $|\mathbf{j}_o \cdot \delta \mathbf{E}| \gg |\mathbf{j}_o \cdot \mathbf{E}_o|$. The main purpose of this paper was to illustrate that high-frequency waves consistently dominate their quasi-static counterparts in the amount they contribute to $(-\mathbf{j} \cdot \mathbf{E})$. In Paper II, we show that the magnitude of $(-\mathbf{j} \cdot \mathbf{E})$ can greatly exceed the energy dissipation rates necessary to regulate the macroscopic shock structure.

However, as we discuss in Paper II, quasi-static fields are not irrelevant. They provide conditions conducive to the growth of the high-frequency waves by differentially decelerating the incident bulk flow. Therefore, they play an integral part in the overall dynamics of collisionless shock waves.

Appendix A: Macroscopic Energy Dissipation

In this appendix, we discuss how we quantified the energy dissipated by the shock on a macroscopic, fluid scale. These estimates were used as a proxy for the total amount of energy the shock needs to dissipate in order to produce the observed changes in entropy and/or kinetic energy density. We then compared the macroscopic dissipation rates to microscopic energy dissipation due to wave-particle interactions (see Appendix B). The quantitative results of this comparison are presented in Paper II.

A1. Thermodynamics

On a fluid, macroscopic scale the two parameters we are concerned with are the change in entropy and kinetic energy density across the shock. We can examine the thermodynamic equation associated with enthalpy, or total internal energy of a system, to determine the energy dissipation associated with a change in entropy. This equation is given by $\Delta \dot{h} = (\rho T) \Delta \dot{s} + C_s^2 \Delta \rho + \Delta \dot{m}_{\text{extr}}$ where $\Delta \dot{h} \equiv$ change in enthalpy density per unit mass (e.g., J m^{-3}), $\rho \equiv$ scalar mass density, $T \equiv$ scalar temperature, $\Delta \dot{s} \equiv$ change in specific entropy

Reflected ions could generate waves.

(e.g., $\text{J } ^\circ\text{K}^{-1} \text{ kg}^{-1}$), $C_s \equiv$ scalar speed of sound, and $\Delta w_{\text{ext}} \equiv$ energy density change due to work done by any external forces. The change in specific entropy has the well known definition given by

$$\Delta s = C_v \ln \left| \frac{\langle P \rangle_{\text{down}}}{\langle P \rangle_{\text{up}}} \left(\frac{\langle \rho \rangle_{\text{up}}}{\langle \rho \rangle_{\text{down}}} \right)^\gamma \right| \quad (\text{A1a})$$

$$C_v = \frac{k_B}{m(\gamma - 1)} \quad (\text{A1b})$$

where $P \equiv$ scalar pressure, $\gamma \equiv$ polytrope index or ratio of specific heats, and the subscript up(down) refers to the initial(final) state [e.g., Gurnett and Bhattacharjee, 2005]. Note that Δs has no dependence on the mechanism that irreversibly transforms energy across the shock ramp. It is only important that energy is dissipated to produce $\Delta s > 0$.

We are concerned with quantifying the amount of energy transformed irreversibly, which relates to the term involving Δs satisfying $\Delta s > 0$. Therefore, we define the macroscopic rate of energy dissipated per unit volume as

$$\dot{\Psi} \equiv (\langle \rho \rangle_{\text{up}} \langle T \rangle_{\text{up}}) \frac{\Delta s}{\Delta \tau} \quad (\text{A2})$$

where $\Delta \tau$ is the shock ramp duration. We used $\dot{\Psi}$ as our first macroscopic energy dissipation estimate. For the 11 bow shock crossings examined, we found $2.5 \times 10^{-6} \lesssim \dot{\Psi} \lesssim 4.0 \times 10^{-4} \mu\text{W m}^{-3}$.

A2. Kinetic Energy Transformation

A second estimate of the macroscopic energy loss is given through a more direct term defined by the change in kinetic energy density across the shock ramp, given by

$$\dot{\kappa} \equiv \frac{1}{2} \frac{\Delta (\rho U_{\text{shn}}^2)}{\Delta \tau} \quad (\text{A3})$$

where U_{shn} is the shock normal speed in the plasma frame. We know that $\dot{\kappa} \Delta \tau$ defines the amount of free energy that has been transformed into other forms across the shock ramp. Therefore, we used $\dot{\kappa}$ as our second macroscopic energy dissipation rate. For the 11 bow shock crossings examined, we found $1.4 \times 10^{-5} \lesssim \dot{\kappa} \lesssim 5.9 \times 10^{-3} \mu\text{W m}^{-3}$.

Appendix B: Microscopic Energy Dissipation

In this appendix, we analytically define our microscopic energy dissipation due to wave-particle interactions and how we compare them to our macroscopic energy dissipation estimates. We provide two different methods for estimating the wave dissipation rate and then discuss the advantages and disadvantages for each.

B1. Poynting's Theorem

Recall from Poynting's theorem that the time rate of change of the energy density of the electromagnetic fields + the rate of electromagnetic energy flux flowing out of a surface = the energy lost due to momentum transfer between particles and fields. This is mathematically expressed as a continuity equation for electromagnetic energy density, given by

$$\partial_t (\mathcal{W}_B + \mathcal{W}_E) + \nabla \cdot \delta \mathbf{S} = -\mathbf{j}_o \cdot \delta \mathbf{E} \quad (\text{B1})$$

where $\mathcal{W}_B \equiv |\delta \mathbf{B}|^2 / (2\mu_o)$, $\mathcal{W}_E \equiv \epsilon_o |\delta \mathbf{E}|^2 / 2$, $\delta \mathbf{S} \equiv (\delta \mathbf{E} \times \delta \mathbf{B}) / \mu_o$, and μ_o is the permeability of free space.

As a supplemental approximation, we estimated the effective resistivity produced by wave-particle interactions, η_{wave} . To compare this to $(-\mathbf{j}_o \cdot \delta \mathbf{E})$, we approximate $\delta \mathbf{E} \approx (\vec{\eta}_{\text{wave}} \cdot \mathbf{j}_o)$. This results in $(-\mathbf{j}_o \cdot \delta \mathbf{E}) \approx (-\mathbf{j}_o \cdot \vec{\eta}_{\text{wave}} \cdot \mathbf{j}_o) \sim (-\eta_{\text{wave}} |\mathbf{j}_o|^2)$. Note that neither $\delta \mathbf{E}$ nor \mathbf{j}_o have any functional dependence upon η_{wave} . Thus, the limitations of the assumptions used to estimate $(-\eta_{\text{wave}} |\mathbf{j}_o|^2)$ have no bearing on our estimates of $(-\mathbf{j}_o \cdot \delta \mathbf{E})$. Recall that $\delta \mathbf{E}$ and $\delta \mathbf{B}$ were transformed into the appropriate reference frame prior to the calculation of $\delta \mathbf{S}$ or either dissipation rate.

In Appendix B2, we introduce the theory behind our resistivity estimates and explain the advantages and disadvantages to using $(-\mathbf{j}_o \cdot \delta \mathbf{E})$ versus $(-\eta_{\text{wave}} |\mathbf{j}_o|^2)$.

B2. Anomalous Resistivity

In a collisional medium, the process that prevents a nonlinearly steepened wave from breaking—energy dissipation—is binary particle collisions. In a collisionless medium, the corresponding mechanisms originally posed a significant problem and are still not quantifiably understood. In one of the first attempts to address this dilemma, *Vedenov* [1963] derived an effective collision frequency, ν_{wave} , from quasi-linear theory that is analogous to Boltzmann's collision operator. The ν_{wave} describes the rate of energy/momentum transfer between electromagnetic fields and charged particles, which can be irreversible and has a net result that is analogous to an effective friction or drag force. The analytical form of ν_{wave} depends upon the dispersion relation for the wave mode producing these so-called wave-particle interactions.

Nonlinear wave steepening in a collisionless shock wave is due to increasing currents [e.g., *Tidman and Northrop*, 1968], produced by the relative drift between electrons and ions that correspond to the magnetic ramp [e.g., *Sagdeev*, 1966; *Gary*, 1981]. Currents can be a source of free energy for instabilities that radiate electromagnetic waves, and instability-driven waves act to reduce the free energy that drives them unstable. Therefore, the waves resulting from current-driven instabilities will act to limit and/or reduce the currents, which led to the original name *anomalous resistivity* [e.g., *Sagdeev*, 1966; *Gary*, 1981].

Our observations consistently show three types of high-frequency electrostatic waves: ion-acoustic waves (IAWs); electrostatic solitary waves (ESWs); and waves due to the electron cyclotron drift instability (ECDI). Recent PIC simulations [e.g., *Muschietti and Lembège*, 2013] have found that the ECDI and IAWs have very similar power spectrums (ignoring the peaks due to the Bernstein modes in the ECDI). The only differences were in the wave polarization and their respective effects on the particle distributions. The IAWs in these simulations began to form electron phase space holes at later times as well. The theories [e.g., *Vedenov*, 1963; *Sagdeev*, 1966; *Gary*, 1981] originally proposed as candidates for collisionless shock energy dissipation involved resistivities due to IAWs. These theories have been indirectly supported in recent observations [*Wilson et al.*, 2007], which showed that the ramp region of collisionless shocks are dominated by large amplitude IAWs. Therefore, we used the IAW solution for the effective collision frequency and corresponding resistivity. Their analytical forms are given by

$$\nu_{\text{IAW}} = \omega_{\text{pe}} \frac{\epsilon_o |\delta E|^2}{2n_e k_B T_e} \quad (\text{B2a})$$

$$\eta_{\text{IAW}} = \frac{\nu_{\text{IAW}}}{\epsilon_o \omega_{\text{pe}}^2} \quad (\text{B2b})$$

where δE is the fluctuating electric field amplitude of the wave, and ν_{IAW} is the effective collision frequency.

Note that equation (B2a) was derived under the assumption of a weakly turbulent plasma, which is not, in general, accurate. One should also note that similar collision frequency estimates for other modes (e.g., the lower hybrid drift instability) can be significantly smaller than for IAWs [e.g., *Labelle and Treumann*, 1988]. Recent wave observations [*Wilson et al.*, 2007, 2010, 2012; *Breneman et al.*, 2013] show that wave amplitudes can be very nonlinear, and thus equations (B2a) and (B2b) may underestimate the effects of wave-particle interactions. In additions, recent Vlasov simulations using realistic mass ratios [*Petkaki et al.*, 2006; *Petkaki and Freeman*, 2008; *Yoon and Lui*, 2006, 2007] have observed momentum transfers that are 2–3 orders of magnitude larger than predicted by equation (B2b). Therefore, we used our estimates of η_{IAW} as a lower bound for the effective resistivity due to wave-particle interactions.

We use two methods to estimate the energy dissipation rate due to wave-particle interactions because each has their own advantages and disadvantages. The assumptions are slightly different for each estimate, and therefore, the resulting uncertainties are different. Note that both estimates, $(-\eta_{\text{IAW}} |\mathbf{j}_o|^2)$ and $(-\mathbf{j}_o \cdot \delta \mathbf{E})$, are independent of each other. Thus, the limitations associated with η_{IAW} have no bearing on our estimate of $(-\mathbf{j}_o \cdot \delta \mathbf{E})$ because we directly estimate \mathbf{j}_o from \mathbf{B}_o and we directly measure $\delta \mathbf{E}$. Below we outline some more limitations for these approximations, but it is important to note that we do not believe these limitations invalidate our results.

Some of the disadvantages of using $\eta_{\text{IAW}} |\mathbf{j}_o|^2$ include, but are not limited to the following: (1) the calculation of ν_{IAW} relies upon our assumption of a dispersion relation; (2) this estimate assumes \mathbf{E} is parallel to \mathbf{j}_o ; (3) this estimate assumes $\mathbf{E} \approx \tilde{\eta}_{\text{IAW}} \cdot \mathbf{j}_o$; and (4) the calculation of ν_{IAW} assumes that the fluctuations are quasi-linear which can result in underestimates for the true momentum exchange rates [e.g., *Petkaki and Freeman*, 2008]. Some of the disadvantages of using $|\mathbf{j}_o \cdot \delta \mathbf{E}|$ include, but are not limited to the following: (1) more reliant

Note! We can estimate J better with MMS

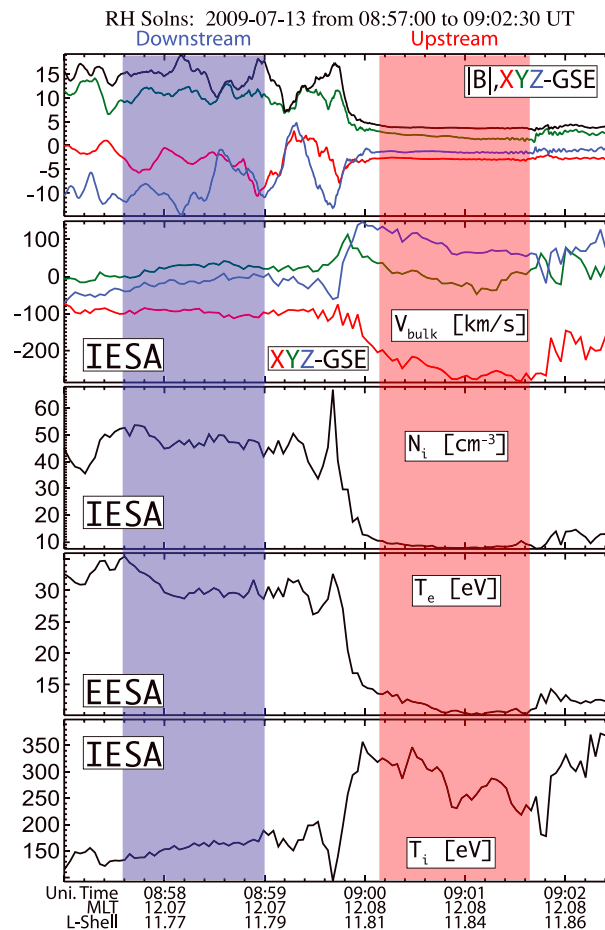


Figure I:5. The figure shows an example bow shock crossing observed by THEMIS-B on 13 July 2009. The panels are as follows: the magnitude of B_o and its GSE components (nT, smoothed, FGM); V_{bulk} in the GSE basis (km/s, IESA); N_i (cm^{-3} , IESA); T_e (eV, EESA); and T_i (eV, IESA). The region shaded in blue defines the downstream (i.e., magnetosheath) and red the upstream (i.e., solar wind).

center was $\sim 08:59:46$ UT and THEMIS-B was at a GSE position of $\sim < +11.5, +1.0, -2.2 > R_E$. Shock waves, by definition, result in an increase in N_i , B_o , T_e , and T_i on the downstream (shocked) side of the transition region. The increase in temperature allows V_{bulk} to decrease to a subsonic value. In Figure I:5 we observed an increase in N_i , B_o , and T_e with corresponding decrease in V_{bulk} , suggesting that this was indeed a shock crossing. However, one can immediately see that the ions appear to be hotter (fifth panel of Figure I:5) on the upstream (unshocked) rather than the downstream (shocked) side. Therefore, the decrease in T_i across the transition region, coupled with the potential for secondary ion contamination (e.g., shock-reflected ions), led us to examine the ion velocity moments in greater detail.

It is well known that the terrestrial bow shock is capable of producing multiple populations of reflected ions [e.g., Bonifazi and Moreno, 1981a, 1981b; Fuselier et al., 1986]. Therefore, we initially assumed that these secondary ions were responsible for some fraction of the error in the ion velocity moments. To test whether ion beams were affecting the upstream ion velocity moments, we examined the entire ion velocity distribution functions in three different reference frames and three different projections. To do this, we converted our observations to phase(velocity) space densities, translated the data into the new reference frame, rotated the data into physically significant coordinate basis (see discussion of Figure I:6), and projected the triangulated results onto the three planes comprising this new coordinate basis.

Figure I:6 shows contours of constant phase space density projected onto three planes (top, middle, and bottom rows) and in three reference frames (first three columns). The three reference frames are defined

upon the accuracy of coordinate basis rotations (e.g., from GSE to NCB); (2) only two components of j_o can be estimated which may have more of an impact on $|j_o \cdot \delta E|$ than $\eta_{iaw} |j_o|^2$; and (3) relies upon the accuracy of the $E/|\delta E|$. Correspondingly, each assumption has its respective advantages. Therefore, we use both methods as a way to test the validity of each.

Appendix C: Removal of Secondary Ions

In this appendix we discuss and provide examples for the removal of secondary ion populations prior to performing moment analysis on the velocity distribution functions.

Onboard particle distribution moments (or moments calculated from telemetered particle distributions) can suffer from inaccuracies due to spacecraft charging [e.g., Génot and Schwartz, 2004; Geach et al., 2005; Davis et al., 2008], multiple species [e.g., Paschmann and Daly, 1998], multiple components [e.g., Wüest et al., 2007], and limited energy ranges (e.g., $V_{Ti} \gtrsim V_{bulk}$). In the following we discuss how we accounted for these potential inaccuracies when examining moments of the velocity distribution functions.

Figure I:5 shows an outbound bow shock crossing observed by THEMIS-B on 13 July 2009. As shown in Table I:1, this shock had $M_f \sim 3.1$ and $\theta_{Bn} \sim 43^\circ$. The shock ramp

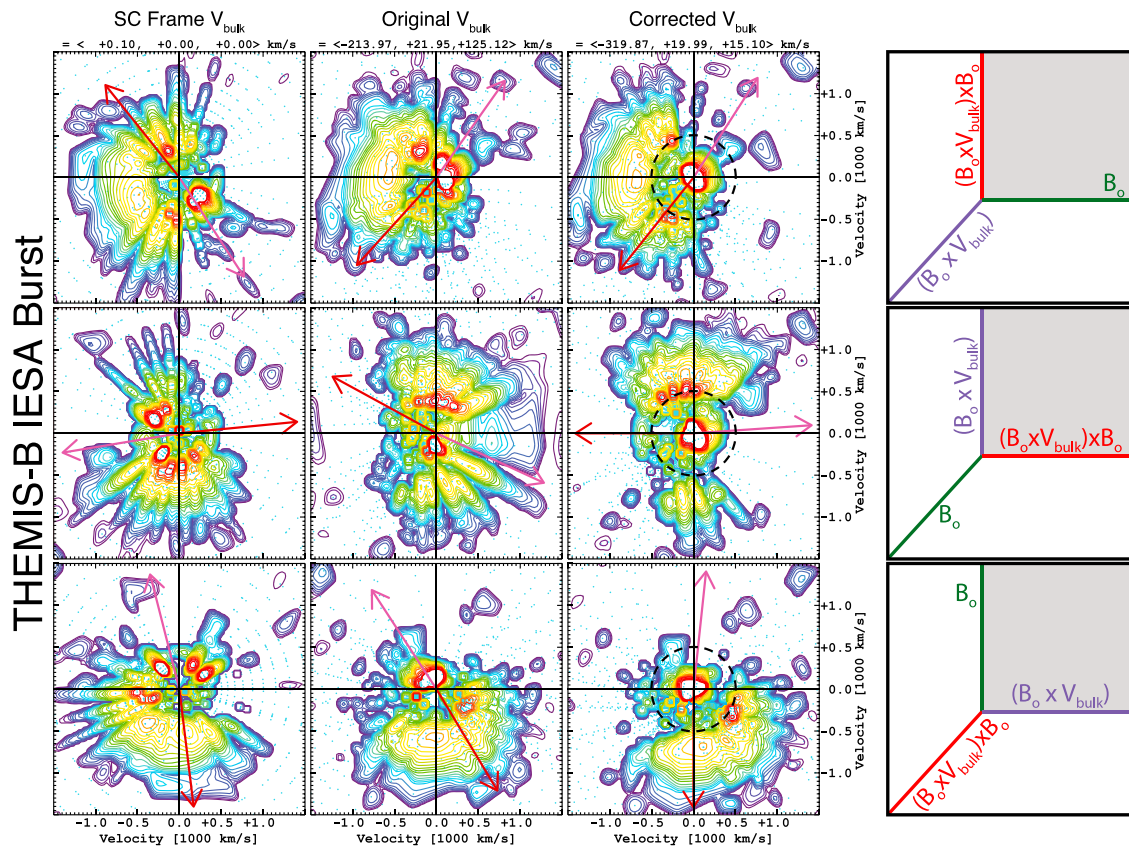


Figure I:6. An example showing an ion particle velocity distribution function, observed by IESA in burst mode, in (first to third columns) three different reference frames projected onto (top, middle, and bottom rows) three different planes. The **shock normal (red arrow)** and **spacecraft-to-Earth (magenta arrow)** vectors are projected onto each contour for reference. The three reference frames are defined by \mathbf{V}_{bulk} at the top of each column. (fourth column) The three different planes defined by the shaded region in the coordinate axes. Each contour plot shows contours of constant phase space density (uniformly scaled from 1×10^{-13} to $1 \times 10^{-7} \text{ s}^3 \text{ cm}^{-3} \text{ km}^{-3}$, where red is high) versus velocity. The velocity axes range from $\pm 1500 \text{ km/s}$, and the crosshairs show the location of the origin. In Figure I:6 (third column), a **circle of constant energy defining the gyrospeed of specularly reflected ions** is shown [e.g., Gosling et al., 1982].

by a velocity relative to the lab frame (roughly the SCF here) shown above the first three columns. These columns represent the following, in order: (1) SCF; (2) level 2 velocity moment rest frame; and (3) incident core solar wind rest frame. The third column shows the velocity distributions in our estimate of the bulk flow rest frame, which defines our estimate of \mathbf{V}_{bulk} . The field-aligned coordinate basis used to define the planes of projection for each row are defined schematically in Figure I:6 (fourth column), where the gray-shaded plane defines the relevant plane for that row. The coordinate basis is dependent upon our estimate of \mathbf{V}_{bulk} and the observed \mathbf{B}_0 (i.e., FGM measurements). These distributions do not assume gyrotropy.

Figure I:6 (third column) represents our adjusted estimates for \mathbf{V}_{bulk} . We determined the new value by plotting the distributions in a manner similar to that shown in Figure I:6, starting in the reference frame defined by the level 2 velocity moment (second column). Then we iteratively change our estimate for \mathbf{V}_{bulk} until the core of the distribution is centered on the origin in all three planes, as seen in the third column. It is important to note that every iteration, thus every change in \mathbf{V}_{bulk} , changes our field-aligned coordinate basis. As can be seen in Figure I:6, the changes in the contour plots can be dramatic. For instance, in the SCF (first column), the secondary population is not obviously a field-aligned beam. However, in the core bulk flow rest frame (third column), the signature of a strong field-aligned beam is obvious. We observed gyrating and field-aligned ion beams upstream (the latter for several minutes) of this shock ramp.

More importantly, if we wish to compare our results to theory, it helps to use a physically meaningful coordinate basis and reference frame. For instance, the third column shows a circle of constant energy (at $\sim 500 \text{ km/s}$) defining the predicted gyrospeed of specularly reflected ions for this shock [e.g., Gosling et al., 1982, equation (6)]. We can use the incident bulk flow velocity as our injection velocity when estimating the gyrospeed for specularly reflected ions at the bow shock because $|\mathbf{V}_{\text{shn}}| \ll |\mathbf{V}_{\text{bulk}}|$ for most events

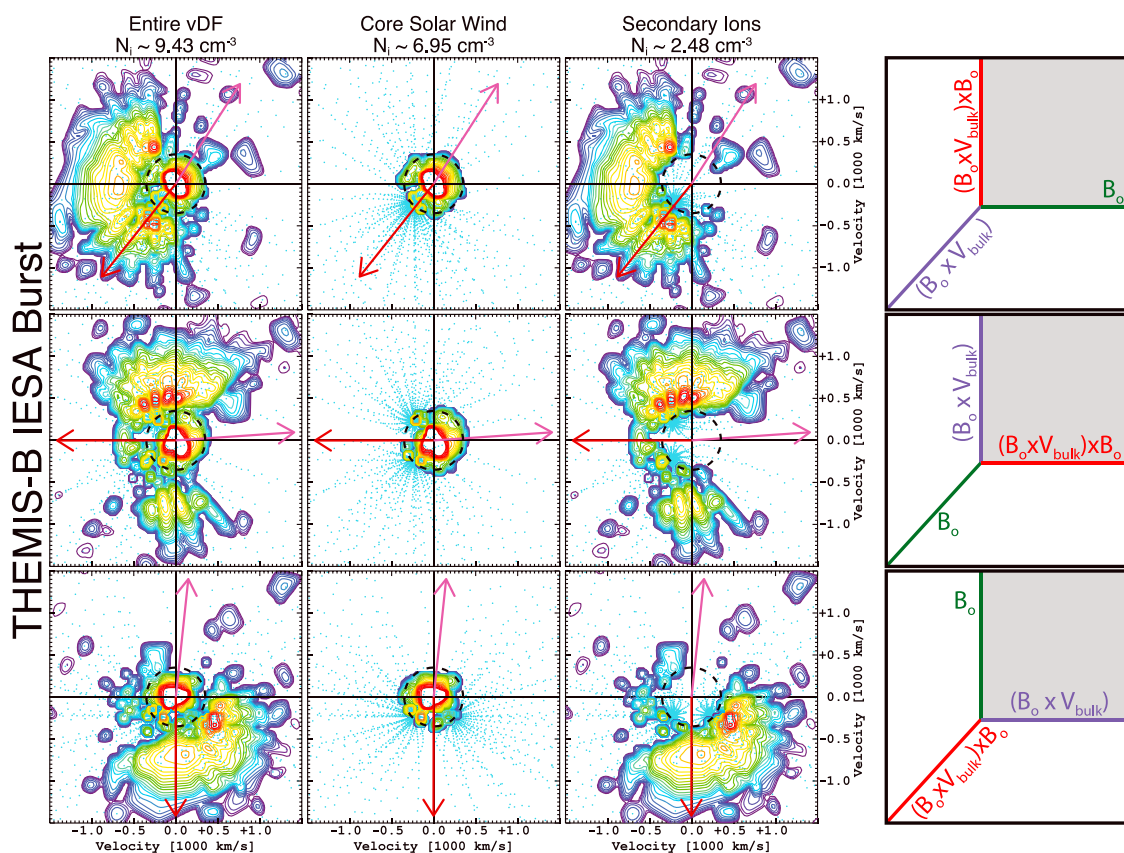


Figure I:7. An example showing **how we separated the incident core solar wind beam from the secondary ion populations using masks**. The distribution shown is the same as that shown in Figure I:6, with the same format except that all columns used the same \mathbf{V}_{bulk} . The circle in each contour plot indicates the energy cutoff used to define the masks to separate between the core solar wind beam and secondary ions. Above the first three columns an estimate of the number density is given for the shown distributions below. Notice that N_r from secondary ions (third column) is $\sim 26\%$ of the total N_i , whereas the N_r from a bi-Maxwellian fit to only the field-aligned beam for this distribution is $\lesssim 2.5\%$.

(e.g., see Table I:1). However, the same does not apply for interplanetary shocks. The features centered on this energy/speed are consistent with the predictions for specularly reflected ions.

Some previous studies have plotted foreshock ion velocity distributions in the SCF; however, Figure I:6 provides an example of why this can lead to confusion or a misinterpretation of the results. Note that the plane of projection in Figure I:6 is dependent upon the definition of \mathbf{V}_{bulk} . If the estimate for \mathbf{V}_{bulk} or the plane of projection is inaccurate, then the projected distribution can be misleading. For instance, when comparing the results for the first plane (Figure I:6, top row), one can see that the core of the second projection looks far more anisotropic than the core in the third projection. If one examines the bottom row of distributions, one can see surprisingly different results between the Figure I:6 (first column) and Figure I:6 (third column). The apparent discrepancies are a consequence of the plotting routines, not a characteristic of the distribution. For more examples of these types of plots, see Wilson *et al.* [2009, 2010, 2012].

After adjusting \mathbf{V}_{bulk} , we created a mask to eliminate all secondary ion populations. We also removed ions within a small cone around the Sun direction to reduce the effects of “UV contamination.” An example can be observed in the third distribution of Figure I:6 (top row) as the intense, narrow beam-like feature in the third quadrant near ~ 500 km/s. We only applied these masks to those distributions with well-defined secondary ion populations. After removing the secondary ions, we recalculated the particle velocity moments. Therefore, these recalculated velocity moments reflect only the core of the ion distribution function.

Figure I:7 shows an example application of how we use these masks to remove secondary ions and estimate reflected ion number densities, N_r . The ion velocity distribution function is the same as the one shown in Figure I:6 and the format of the figure is the same. Figure I:7 (first column) is identical to Figure I:6 (third column) except for the circle of constant energy/speed, which is now at ~ 350 km/s. The second and third

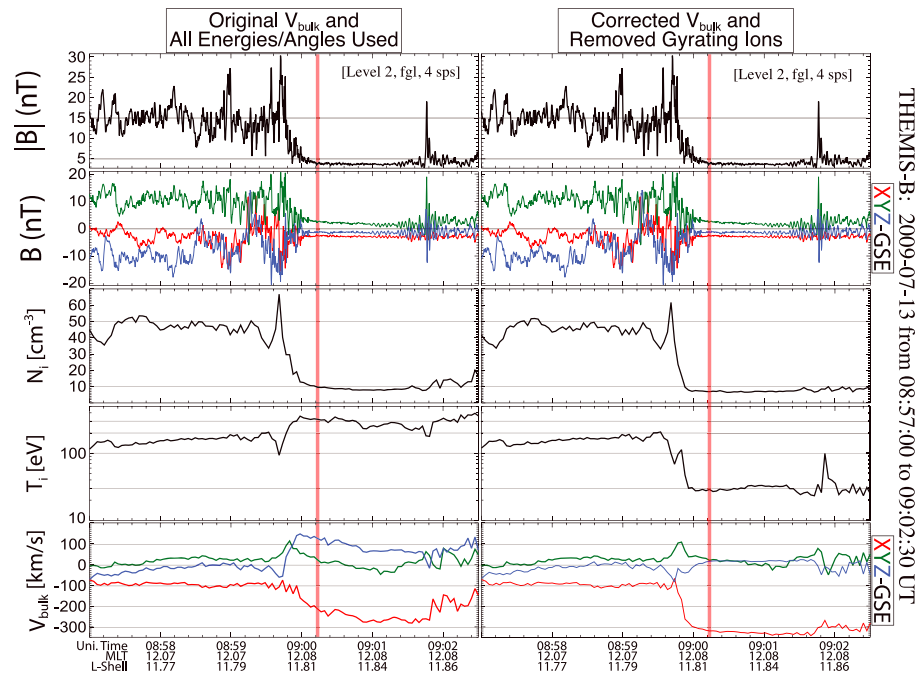


Figure I:8. The comparison between the level 2 velocity moments (left-hand column) and our estimates after removing the secondary ion beams (right-hand column). The panels are as follows: $|B_o|$ (nT, 4 sps, FGM); B_o in the GSE basis (nT, 4 sps, FGM); N_i (cm^{-3} , IESA); T_i (eV, IESA); and V_{bulk} in the GSE basis (km/s, IESA). The magnetic fields are identical in each column. The horizontal gray lines in each panel are to help the reader compare differences between the two results.

columns show the results of our masks, where the former removes everything but the incident solar wind core and the latter keeps only the secondary ions. Above each column are the number density estimates for the shown velocity distribution function.

The secondary ions in Figure I:7 (third column) show features consistent with field-aligned and intermediate/diffuse ions [e.g., Paschmann *et al.*, 1981]. We fit bi-Maxwellian distributions to just the field-aligned beam and found $N_b \sim 0.2 \text{ cm}^{-3}$, which is only $\sim 2.4\%$ of the total N_i for this distribution. This bow shock crossing (on 13 July 2009) had the highest relative and absolute values of N_b with $N_b/\langle N_i \rangle_{\text{up}} \sim 1\text{--}5\%$. For all the other bow shock crossings, this ratio was reduced to $< 1\%$. If we include all the secondary ions to estimate N_r , then we find $N_r/N_i \sim 26\%$ for this distribution and ranging from $\sim 20\text{--}40\%$ for all the other bow shock crossings. We observe a general trend that the relative and absolute values of N_r decrease with increasing distance from the shock ramp (i.e., the largest values are usually found immediately upstream in the foot).

Let us define $\langle N_r/N_i \rangle$ as the average relative number density of reflected ions observed upstream of any given shock ramp. We use an average because the values can vary radically in one bow shock crossing from distribution to distribution (e.g., from $\sim 3\%$ to $> 40\%$). We find a general agreement with theory in that all the events with $\langle N_r/N_i \rangle > 30\%$ had $M_f/M_{\text{cr},2} \geq 2.3$ and $M_f \geq 3.1$. We also found a general increasing trend in $\langle N_r/N_i \rangle$ with increasing M_f , $M_f/M_{\text{cr},1}$, and $M_f/M_{\text{cr},2}$. However, we observed some exceptions/outliers. For instance, the third crossing on 5 September 2009 has $M_f > 5$ and $M_f/M_{\text{cr},2} \sim 4.7$ but had $\langle N_r/N_i \rangle < 5\%$. However, our immediate concern is the effect that the secondary ions have on our velocity moment estimates.

We show an example comparison between the original level 2 velocity moments and the core only estimates in Figure I:8. The time range shown is the same as in Figure I:5. The red-shaded region corresponds to the time range of the ion velocity distribution shown in Figure I:6. The results for T_i and V_{bulk} show dramatic differences, whereas N_i shows only minor differences in the upstream. The most important observations are that T_i now increases across the shock ramp and that $|V_{\text{bulk}}|$ shows differences of up to $\sim 30\%$. Not only did we observe large differences in $|V_{\text{bulk}}|$, one can see that there are significant changes in the flow direction as well.

There is a large amplitude magnetic fluctuations observed near $\sim 09:02$ UT, which causes a deflection of the core \mathbf{V}_{bulk} . We observed heating of the core ions and electrons near this structure as well. A comparison between the N_i plots in Figure 1:8 shows that the secondary ions were enhanced near this structure. When we examined the ion distributions (e.g., see Figure 1:6), we observed enhanced field-aligned and gyrophase-bunched ions near these fluctuations, consistent with recent observations [Wilson *et al.*, 2013b].

Upon examination of the results shown in Table 1:1, one can see that a few events have $\langle N_i \rangle_{\text{down}} / \langle N_i \rangle_{\text{up}} > 4$. There are many possible explanations for this, including but not limited to the following: (1) $\langle N_i \rangle_{\text{up}}$ does not include reflected particles; (2) the spacecraft velocity had a significant component along the shock plane; (3) time variations due to single spacecraft observations; (4) inaccuracies in velocity moments due to $V_{Ti} \gtrsim V_{\text{bulk}}$; (5) and others. Note that events with $\langle N_i \rangle_{\text{down}} / \langle N_i \rangle_{\text{up}} > 4$ are only in violation of a time stationary neutral fluid approximations. If, for instance, the bow shock was being increasingly compressed as the spacecraft passed through the downstream region, one might expect $\langle N_i \rangle_{\text{down}} / \langle N_i \rangle_{\text{up}} > 4$.

Acknowledgments

We would like to thank A.F. Viñas, D. Bryant, D.A. Roberts, R.T. Wicks, R. Lysak, and M.L. Goldstein for useful discussions of the fundamental physics involved in our study. The work was partially supported by Wind MO and DA grants. The French involvement (SCM instruments) on THEMIS are supported by CNES and CNRS-INSU. The data used in this paper and the associated calibration software can be found at <http://themis.ssl.berkeley.edu/index.shtml>.

Yuming Wang thanks the reviewers for their assistance in evaluating this paper.

References

- Auster, H. U., et al. (2008), The THEMIS fluxgate magnetometer, *Space Sci. Rev.*, **141**, 235–264, doi:10.1007/s11214-008-9365-9.
- Bale, S. D., et al. (2005), Quasi-perpendicular shock structure and processes, *Space Sci. Rev.*, **118**, 161–203, doi:10.1007/s11214-005-3827-0.
- Bonifazi, C., and G. Moreno (1981a), Reflected and diffuse ions backstreaming from the Earth's bow shock: 1. Basic properties, *J. Geophys. Res.*, **86**, 4397–4413, doi:10.1029/JA086iA06p04397.
- Bonifazi, C., and G. Moreno (1981b), Reflected and diffuse ions backstreaming from the Earth's bow shock: 2. Origin, *J. Geophys. Res.*, **86**, 4405–4414, doi:10.1029/JA086iA06p04405.
- Bonnell, J. W., F. S. Mozer, G. T. Delory, A. J. Hull, R. E. Ergun, C. M. Cully, V. Angelopoulos, and P. R. Harvey (2008), The Electric Field Instrument (EFI) for THEMIS, *Space Sci. Rev.*, **141**, 303–341, doi:10.1007/s11214-008-9469-2.
- Breneman, A., C. Cattell, K. Kersten, A. Paradise, S. Schreiner, P. J. Kellogg, K. Goetz, and L. B. Wilson III (2013), STEREO and Wind observations of intense cyclotron harmonic waves at the Earth's bow shock and inside the magnetosheath, *J. Geophys. Res. Space Physics*, **118**, 7654–7664, doi:10.1002/2013JA019372.
- Bryant, D. A. (1999), *Electron Acceleration in the Aurora and Beyond*, Institute of Physics Publishing, Bristol and Philadelphia, Pa.
- Cairns, I. H., and B. F. McMillan (2005), Electron acceleration by lower hybrid waves in magnetic reconnection regions, *Phys. Plasmas*, **12**, 102,110, doi:10.1063/1.2080567.
- Coroniti, F. V. (1970), Dissipation discontinuities in hydromagnetic shock waves, *J. Plasma Phys.*, **4**, 265, doi:10.1017/S0022377800004992.
- Cully, C. M., R. E. Ergun, K. Stevens, A. Nannari, and J. Westfall (2008), The THEMIS digital fields board, *Space Sci. Rev.*, **141**, 343–355, doi:10.1007/s11214-008-9417-1.
- Davidson, R. C., and J. M. Ogden (1975), Electromagnetic ion cyclotron instability driven by ion energy anisotropy in high-beta plasmas, *Phys. Fluids*, **18**, 1045–1050, doi:10.1063/1.861253.
- Davis, V. A., M. J. Mandell, and M. F. Thomsen (2008), Representation of the measured geosynchronous plasma environment in spacecraft charging calculations, *J. Geophys. Res.*, **113**, A10204, doi:10.1029/2008JA013116.
- Dimmock, A. P., M. A. Balikhin, V. V. Krasnoselskikh, S. N. Walker, S. D. Bale, and Y. Hobara (2012), A statistical study of the cross-shock electric potential at low Mach number, quasi-perpendicular bow shock crossings using Cluster data, *J. Geophys. Res.*, **117**, A02210, doi:10.1029/2011JA017089.
- Eastwood, J. P., S. D. Bale, F. S. Mozer, and A. J. Hull (2007), Contributions to the cross shock electric field at a quasiperpendicular collisionless shock, *Geophys. Res. Lett.*, **34**, L17104, doi:10.1029/2007GL030610.
- Edmiston, J. P., and C. F. Kennel (1984), A parametric survey of the first critical Mach number for a fast MHD shock, *J. Plasma Phys.*, **32**, 429–441.
- Fishman, F. J., A. R. Kantrowitz, and H. E. Petschek (1960), Magnetohydrodynamic shock wave in a collision-free plasma, *Rev. Modern Phys.*, **32**, 959–966, doi:10.1103/RevModPhys.32.959.
- Fuselier, S. A., M. F. Thomsen, J. T. Gosling, S. J. Bame, and C. T. Russell (1986), Gyration and intermediate ion distributions upstream from the Earth's bow shock, *J. Geophys. Res.*, **91**, 91–99, doi:10.1029/JA091iA01p00091.
- Gary, S. P. (1981), Microinstabilities upstream of the Earth's bow shock—A brief review, *J. Geophys. Res.*, **86**, 4331–4336, doi:10.1029/JA086iA06p04331.
- Geach, J., S. J. Schwartz, V. Génot, O. Moullard, A. Lahiff, and A. N. Fazakerley (2005), A corrector for spacecraft calculated electron moments, *Ann. Geophys.*, **23**, 931–943, doi:10.5194/angeo-23-931-2005.
- Génot, V., and S. Schwartz (2004), Spacecraft potential effects on electron moments derived from a perfect plasma detector, *Ann. Geophys.*, **22**, 2073–2080, doi:10.5194/angeo-22-2073-2004.
- Gosling, J. T., M. F. Thomsen, S. J. Bame, W. C. Feldman, G. Paschmann, and N. Sckopke (1982), Evidence for specularly reflected ions upstream from the quasi-parallel bow shock, *Geophys. Res. Lett.*, **9**, 1333–1336, doi:10.1029/GL009i012p01333.
- Greenstadt, E. W., and M. M. Mellott (1987), Plasma wave evidence for reflected ions in front of subcritical shocks—ISEE 1 and 2 observations, *J. Geophys. Res.*, **92**, 4730–4734, doi:10.1029/JA092iA05p04730.
- Gurgiolo, C., G. K. Parks, B. H. Mauk, K. A. Anderson, R. P. Lin, H. Reme, and C. S. Lin (1981), Non-E \times B ordered ion beams upstream of the Earth's bow shock, *J. Geophys. Res.*, **86**, 4415–4424, doi:10.1029/JA086iA06p04415.
- Gurnett, D. A., and A. Bhattacharjee (2005), *Introduction to Plasma Physics: With Space and Laboratory Applications*, Cambridge Univ. Press, Cambridge, U. K.
- Hao, Y., Q. Lu, X. Gao, C. Huang, S. Lu, L. Shan, and S. Wang (2014), He²⁺ dynamics and ion cyclotron waves in the downstream of quasi-perpendicular shocks: 2-D hybrid simulations, *J. Geophys. Res. Space Physics*, **119**, 3225–3236, doi:10.1002/2013JA019717.
- Hellinger, P., P. Trávníček, B. Lembège, and P. Savoini (2007), Emission of nonlinear whistler waves at the front of perpendicular supercritical shocks: Hybrid versus full particle simulations, *Geophys. Res. Lett.*, **34**, L14109, doi:10.1029/2007GL030239.
- Hoppe, M. M., C. T. Russell, L. A. Frank, T. E. Eastman, and E. W. Greenstadt (1981), Upstream hydromagnetic waves and their association with backstreaming ion populations—ISEE 1 and 2 observations, *J. Geophys. Res.*, **86**, 4471–4492, doi:10.1029/JA086iA06p04471.
- Hull, A. J., J. D. Scudder, L. A. Frank, W. R. Paterson, and M. G. Kivelson (1998), Electron heating and phase space signatures at strong and weak quasi-perpendicular shocks, *J. Geophys. Res.*, **103**, 2041–2054, doi:10.1029/97JA03058.

- Hull, A. J., J. D. Scudder, R. J. Fitzenreiter, K. W. Ogilvie, J. A. Newbury, and C. T. Russell (2000), Electron temperature and de Hoffmann-Teller potential change across the Earth's bow shock: New results from ISEE 1, *J. Geophys. Res.*, *105*, 20,957–20,972, doi:10.1029/2000JA900049.
- Hull, A. J., J. D. Scudder, D. E. Larson, and R. Lin (2001), Electron heating and phase space signatures at supercritical, fast mode shocks, *J. Geophys. Res.*, *106*, 15,711–15,734, doi:10.1029/2001JA900001.
- Hull, A. J., L. Muschietti, M. Oka, D. E. Larson, F. S. Mozer, C. C. Chaston, J. W. Bonnell, and G. B. Hospodarsky (2012), Multiscale whistler waves within Earth's perpendicular bow shock, *J. Geophys. Res.*, *117*, A12104, doi:10.1029/2012JA017870.
- Jackson, J. D. (1998), *Classical Electrodynamics*, 3rd ed., John Wiley, New York.
- Kellogg, P. J. (1962), Flow of plasma around the Earth, *J. Geophys. Res.*, *67*, 3805–3811, doi:10.1029/JZ067i010p03805.
- Kennel, C. F. (1987), Critical Mach numbers in classical magnetohydrodynamics, *J. Geophys. Res.*, *92*, 13,427–13,437, doi:10.1029/JA092iA12p13427.
- Kennel, C. F., J. P. Edmiston, and T. Hada (1985), A quarter century of collisionless shock research, in *Collisionless Shocks in the Heliosphere: A Tutorial Review*, *Geophys. Monogr. Ser.*, vol. 34, edited by R. G. Stone and B. T. Tsurutani, pp. 1–36, AGU, Washington, D. C., doi:10.1029/GM034p0001.
- Koval, A., and A. Szabo (2008), Modified “Rankine-Hugoniot” shock fitting technique: Simultaneous solution for shock normal and speed, *J. Geophys. Res.*, *113*, A10110, doi:10.1029/2008JA013337.
- Krasnoselskikh, V. V., B. Lembège, P. Savoini, and V. V. Lobzin (2002), Nonstationarity of strong collisionless quasiperpendicular shocks: Theory and full particle numerical simulations, *Phys. Plasmas*, *9*, 1192–1209, doi:10.1063/1.1457465.
- Krauss-Varban, D., and N. Omid (1991), Structure of medium Mach number quasi-parallel shocks—Upstream and downstream waves, *J. Geophys. Res.*, *96*, 17,715–17,731, doi:10.1029/91JA01545.
- Labelle, J., and R. A. Treumann (1988), Plasma waves at the dayside magnetopause, *Space Sci. Rev.*, *47*, 175–202, doi:10.1007/BF00223240.
- Lapenta, G., M. Goldman, D. Newman, S. Markidis, and A. Divin (2014), Electromagnetic energy conversion in downstream fronts from three dimensional kinetic reconnection^Q, *Phys. Plasmas*, *21*(5), 055,702, doi:10.1063/1.4872028.
- Le Contel, O., et al. (2008), First results of the THEMIS search coil magnetometers, *Space Sci. Rev.*, *141*, 509–534, doi:10.1007/s11214-008-9371-y.
- Lu, Q. M., and S. Wang (2006), Electromagnetic waves downstream of quasi-perpendicular shocks, *J. Geophys. Res.*, *111*, A05204, doi:10.1029/2005JA011319.
- Matsukiyo, S., and M. Scholer (2006), On microinstabilities in the foot of high Mach number perpendicular shocks, *J. Geophys. Res.*, *111*, A06104, doi:10.1029/2005JA011409.
- Mazelle, C., B. Lembège, A. Morgenthaler, K. Meziane, T. S. Horbury, V. Génot, E. A. Lucek, and I. Dandouras (2010), Self-reformation of the quasi-perpendicular shock: CLUSTER observations, *AIP Conf. Proc.*, *1216*, 471–474, doi:10.1063/1.3395905.
- McFadden, J. P., C. W. Carlson, D. Larson, M. Ludlam, R. Abiad, B. Elliott, P. Turin, M. Marckwordt, and V. Angelopoulos (2008a), The THEMIS ESA plasma instrument and in-flight calibration, *Space Sci. Rev.*, *141*, 277–302, doi:10.1007/s11214-008-9440-2.
- McFadden, J. P., C. W. Carlson, D. Larson, J. Bonnell, F. Mozer, V. Angelopoulos, K.-H. Glassmeier, and U. Auster (2008b), THEMIS ESA first science results and performance issues, *Space Sci. Rev.*, *141*, 477–508, doi:10.1007/s11214-008-9433-1.
- Mellott, M. M., and E. W. Greenstadt (1984), The structure of oblique subcritical bow shocks—ISEE 1 and 2 observations, *J. Geophys. Res.*, *89*, 2151–2161, doi:10.1029/JA089iA04p02151.
- Meziane, K., et al. (1997), Wind observation of gyrating-like ion distributions and low frequency waves upstream from the Earth's bow shock, *Adv. Space Res.*, *20*, 703–706, doi:10.1016/S0273-1177(97)00459-6.
- Mitchell, J. J., and S. J. Schwartz (2014), Isothermal magnetosheath electrons due to nonlocal electron cross talk, *J. Geophys. Res.*, *119*, 1080–1093, doi:10.1002/2013JA019211.
- Mitchell, J. J., S. J. Schwartz, and U. Auster (2012), Electron cross talk and asymmetric electron distributions near the Earth's bowshock, *Ann. Geophys.*, *30*, 503–513, doi:10.5194/angeo-30-503-2012.
- Mozer, F. S., and D. Sundkvist (2013), Electron demagnetization and heating in quasi-perpendicular shocks, *J. Geophys. Res.*, *118*, 5415–5420, doi:10.1002/jgra.50534.
- Muschietti, L., and B. Lembège (2013), Microturbulence in the electron cyclotron frequency range at perpendicular supercritical shocks, *J. Geophys. Res. Space Physics*, *118*, 2267–2285, doi:10.1002/jgra.50224.
- Paschmann, G., and P. W. Daly (1998), Analysis methods for multi-spacecraft data, *ISSI Scientific Rep. Series SR-001*, ESA/ISSI, International Space Science Institute, Bern, Switzerland.
- Paschmann, G., N. Sckopke, I. Papamastorakis, J. R. Asbridge, S. J. Bame, and J. T. Gosling (1981), Characteristics of reflected and diffuse ions upstream from the Earth's bow shock, *J. Geophys. Res.*, *86*, 4355–4364, doi:10.1029/JA086iA06p04355.
- Penrose, O. (1979), Foundations of statistical mechanics, *Rep. Prog. Phys.*, *42*, 1937–2006, doi:10.1088/0034-4885/42/12/002.
- Petkaki, P., and M. P. Freeman (2008), Nonlinear dependence of anomalous ion-acoustic resistivity on electron drift velocity, *Astrophys. J.*, *686*, 686–693, doi:10.1086/590654.
- Petkaki, P., M. P. Freeman, T. Kirk, C. E. J. Watt, and R. B. Horne (2006), Anomalous resistivity and the nonlinear evolution of the ion-acoustic instability, *J. Geophys. Res.*, *111*, A01205, doi:10.1029/2004JA010793.
- Petschek, H. E. (1958), Aerodynamic dissipation, *Rev. Mod. Phys.*, *30*, 966–974, doi:10.1103/RevModPhys.30.966.
- Roux, A., O. Le Contel, C. Coillot, A. Bouabdellah, B. de La Porte, D. Alison, S. Ruocco, and M. C. Vassal (2008), The search coil magnetometer for THEMIS, *Space Sci. Rev.*, *141*, 265–275, doi:10.1007/s11214-008-9455-8.
- Sagdeev, R. Z. (1966), Cooperative phenomena and shock waves in collisionless plasmas, in *Reviews of Plasma Physics*, vol. 4, edited by M. A. Leontovich, 23 pp., Consultants Bur., New York.
- Scholer, M., H. Kucharek, and I. Shinohara (2003), Short large-amplitude magnetic structures and whistler wave precursors in a full-particle quasi-parallel shock simulation, *J. Geophys. Res.*, *108*, 1273, doi:10.1029/2002JA009820.
- Schwartz, S. J., E. Henley, J. Mitchell, and V. Krasnoselskikh (2011), Electron temperature gradient scale at collisionless shocks, *Phys. Rev. Lett.*, *107*, 215,002, doi:10.1103/PhysRevLett.107.215002.
- Scudder, J. D., T. L. Aggson, A. Mangeney, C. Lacombe, and C. C. Harvey (1986a), The resolved layer of a collisionless, high beta, supercritical, quasi-perpendicular shock wave: I. Rankine-Hugoniot geometry, currents, and stationarity, *J. Geophys. Res.*, *91*, 11,019–11,052, doi:10.1029/JA091iA10p11019.
- Scudder, J. D., T. L. Aggson, A. Mangeney, C. Lacombe, and C. C. Harvey (1986b), The resolved layer of a collisionless, high beta, supercritical, quasi-perpendicular shock wave: II. Dissipative fluid electrodynamics, *J. Geophys. Res.*, *91*, 11,053–11,073, doi:10.1029/JA091iA10p11053.
- Scudder, J. D., A. Mangeney, C. Lacombe, C. C. Harvey, and C. S. Wu (1986c), The resolved layer of a collisionless, high beta, supercritical, quasi-perpendicular shock wave: III. Vlasov electrodynamics, *J. Geophys. Res.*, *91*, 11,075–11,097, doi:10.1029/JA091iA10p11075.

- Shu, F. H. (1992), *Physics of Astrophysics*, vol. 2, University Science Books, Mill Valley, Calif.
- Spitzer, L., and R. Härm (1953), Transport phenomena in a completely ionized gas, *Phys. Rev.*, **89**, 977–981, doi:10.1103/PhysRev.89.977.
- Su, Y., Q. Lu, X. Gao, C. Huang, and S. Wang (2012), Ion dynamics at supercritical quasi-parallel shocks: Hybrid simulations, *Phys. Plasmas*, **19**(9), 092108, doi:10.1063/1.4752219.
- Sundkvist, D., V. Krasnoselskikh, S. D. Bale, S. J. Schwartz, J. Soucek, and F. Mozer (2012), Dispersive nature of high Mach number collisionless plasma shocks: Poynting flux of oblique whistler waves, *Phys. Rev. Lett.*, **108**, 025002, doi:10.1103/PhysRevLett.108.025002.
- Tidman, D. A., and N. A. Krall (1971), *Shock Waves in Collisionless Plasmas*, John Wiley, New York.
- Tidman, D. A., and T. G. Northrop (1968), Emission of plasma waves by the Earth's bow shock, *J. Geophys. Res.*, **73**, 1543–1553, doi:10.1029/JA073i005p01543.
- Treumann, R. A. (2009), Fundamentals of collisionless shocks for astrophysical application. 1. Non-relativistic shocks, *Astron. Astrophys. Rev.*, **17**, 409–535, doi:10.1007/s00159-009-0024-2.
- Tsubouchi, K., and B. Lembège (2004), Full particle simulations of short large-amplitude magnetic structures (SLAMS) in quasi-parallel shocks, *J. Geophys. Res.*, **109**, A02114, doi:10.1029/2003JA010014.
- Vedenov, A. A. (1963), Quasi-linear plasma theory (theory of a weakly turbulent plasma), *J. Nucl. Energy*, **5**, 169–186, doi:10.1088/0368-3281/5/3/305.
- Vinas, A. F., and J. D. Scudder (1986), Fast and optimal solution to the 'Rankine-Hugoniot problem', *J. Geophys. Res.*, **91**, 39–58, doi:10.1029/JA091iA01p00039.
- Wilson, L. B., III, C. Cattell, P. J. Kellogg, K. Goetz, K. Kersten, L. Hanson, R. MacGregor, and J. C. Kasper (2007), Waves in interplanetary shocks: A wind/waves study, *Phys. Rev. Lett.*, **99**(4), 041101, doi:10.1103/PhysRevLett.99.041101.
- Wilson, L. B., III, C. A. Cattell, P. J. Kellogg, K. Goetz, K. Kersten, J. C. Kasper, A. Szabo, and K. Meziane (2009), Low-frequency whistler waves and shocklets observed at quasi-perpendicular interplanetary shocks, *J. Geophys. Res.*, **114**, A10106, doi:10.1029/2009JA014376.
- Wilson, L. B., III, C. A. Cattell, P. J. Kellogg, K. Goetz, K. Kersten, J. C. Kasper, A. Szabo, and M. Wilber (2010), Large-amplitude electrostatic waves observed at a supercritical interplanetary shock, *J. Geophys. Res.*, **115**, A12104, doi:10.1029/2010JA015332.
- Wilson, L. B., III, et al. (2012), Observations of electromagnetic whistler precursors at supercritical interplanetary shocks, *Geophys. Res. Lett.*, **39**, L08109, doi:10.1029/2012GL051581.
- Wilson, L. B., III, et al. (2013a), Electromagnetic waves and electron anisotropies downstream of supercritical interplanetary shocks, *J. Geophys. Res. Space Physics*, **118**(1), 5–16, doi:10.1029/2012JA018167.
- Wilson, L. B., III, et al. (2013b), Shocklets, SLAMS, and field-aligned ion beams in the terrestrial foreshock, *J. Geophys. Res. Space Physics*, **118**(3), 957–966, doi:10.1029/2012JA018186.
- Wilson, L. B., III, D. G. Sibeck, A. W. Breneman, O. Le Contel, C. Cully, D. L. Turner, V. Angelopoulos, and D. M. Malaspina (2014), Quantified energy dissipation rates in the terrestrial bow shock: 2. Waves and dissipation, *J. Geophys. Res. Space Physics*, doi:10.1002/2014JA019930.
- Wu, C. S., et al. (1984), Microinstabilities associated with a high Mach number, perpendicular bow shock, *Space Sci. Rev.*, **37**, 63–109, doi:10.1007/BF00213958.
- Wüst, M., D. S. Evans, and R. von Steiger (eds.) (2007), *Calibration of Particle Instruments in Space Physics*, ESA Publications Division, Keplerlaan 1, 2200 AG Noordwijk, Netherlands.
- Yang, Z. W., B. Lembège, and Q. M. Lu (2011), Impact of the nonstationarity of a supercritical perpendicular collisionless shock on the dynamics and energy spectra of pickup ions, *J. Geophys. Res.*, **116**, A08216, doi:10.1029/2010JA016360.
- Yoon, P. H., and A. T. Y. Lui (2006), Quasi-linear theory of anomalous resistivity, *J. Geophys. Res.*, **111**, A02203, doi:10.1029/2005JA011482.
- Yoon, P. H., and A. T. Y. Lui (2007), Anomalous resistivity by fluctuation in the lower-hybrid frequency range, *J. Geophys. Res.*, **112**, A06207, doi:10.1029/2006JA012209.

Erratum

In the originally published version of this article, the heading of section 6 contained a typographical error. The heading has been corrected, and the current version may be considered the authoritative version of record.